

See discussions, stats, and author profiles for this publication at: <https://www.researchgate.net/publication/235785833>

# Synthesis and Preliminary Evaluation in Tumor Bearing Mice of New 18 F-Labeled Arylsulfone Matrix Metalloproteinase Inhibitors as Tracers for Positron Emission Tomography

ARTICLE *in* JOURNAL OF MEDICINAL CHEMISTRY · MARCH 2013

Impact Factor: 5.45 · DOI: 10.1021/jm4001743 · Source: PubMed

---

CITATIONS

4

---

READS

115

20 AUTHORS, INCLUDING:



**Giovanna Esposito**

Università degli Studi di Torino

13 PUBLICATIONS 531 CITATIONS

SEE PROFILE



**Antonietta Bartoli**

Italian National Research Council

16 PUBLICATIONS 282 CITATIONS

SEE PROFILE

# Synthesis and Preliminary Evaluation in Tumor Bearing Mice of New $^{18}\text{F}$ -Labeled Arylsulfone Matrix Metalloproteinase Inhibitors as Tracers for Positron Emission Tomography

Francesca Casalini,<sup>†,▲</sup> Lorenza Fugazza,<sup>‡,▲</sup> Giovanna Esposito,<sup>§</sup> Claudia Cabella,<sup>||</sup> Chiara Brioschi,<sup>||</sup> Alessia Cordaro,<sup>||</sup> Luca D'Angeli,<sup>§</sup> Antonietta Bartoli,<sup>§</sup> Azzurra M. Filannino,<sup>‡</sup> Concetta V. Gringeri,<sup>†</sup> Dario L. Longo,<sup>§</sup> Valeria Muzio,<sup>‡</sup> Elisa Nuti,<sup>⊥</sup> Elisabetta Orlandini,<sup>⊥</sup> Gianluca Figlia,<sup>▽</sup> Angelo Quattrini,<sup>▽</sup> Lorenzo Tei,<sup>†</sup> Giuseppe Digilio,<sup>\*,†,§</sup> Armando Rossello,<sup>\*,⊥</sup> and Alessandro Maiocchi<sup>||</sup>

<sup>†</sup>Department of Science and Technological Innovation, Università del Piemonte Orientale "Amedeo Avogadro", Viale T. Michel 11, I-15121 Alessandria, Italy

<sup>‡</sup>Research and Development, Advanced Accelerator Applications, Via Ribes 5, I-10010 Colletterto Giacosa (TO), Italy

<sup>§</sup>Molecular Imaging Centre, University of Torino, Via Nizza 52, I-10126 Torino, Italy

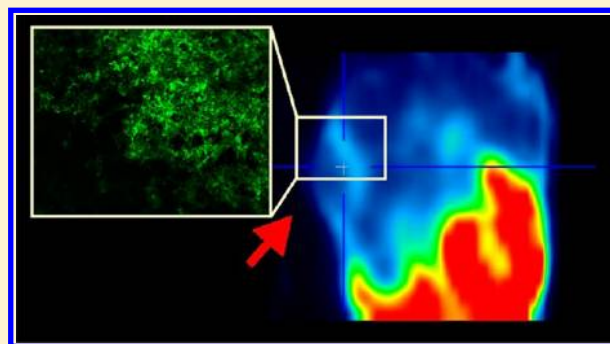
<sup>||</sup>Centro Ricerche Bracco, Bracco Imaging S.p.A., Via Ribes 5, I-10010 Colletterto Giacosa (TO), Italy

<sup>⊥</sup>Department of Pharmacy, University of Pisa, Via Bonanno 6, I-56126 Pisa, Italy

<sup>▽</sup>Institute of Experimental Neurology, Division of Neuroscience, San Raffaele Scientific Institute, Via Olgettina 58, 20132 Milan, Italy

## **S** Supporting Information

**ABSTRACT:** New fluorinated, arylsulfone-based matrix metalloproteinase (MMP) inhibitors containing carboxylate as the zinc binding group were synthesized as radiotracers for positron emission tomography. Inhibitors were characterized by  $K_i$  for MMP-2 in the nanomolar range and by a fair selectivity for MMP-2/9/12/13 over MMP-1/3/14. Two of these compounds were obtained in the  $^{18}\text{F}$ -radiolabeled form, with radiochemical purity and yield suitable for preliminary studies in mice xenografted with a human U-87 MG glioblastoma. Target density in xenografts was assessed by Western blot, yielding  $B_{\text{max}}/K_d = 14$ . The biodistribution of the tracer was dominated by liver uptake and hepatobiliary clearance. Tumor uptake of  $^{18}\text{F}$ -labeled MMP inhibitors was about 30% that of [ $^{18}\text{F}$ ]fluorodeoxyglucose. Accumulation of radioactivity within the tumor periphery colocalized with MMP-2 activity (evaluated by in situ zymography). However, specific tumor uptake accounted for only 18% of total uptake. The aspecific uptake was ascribed to the high binding affinity between the radiotracer and serum albumin.



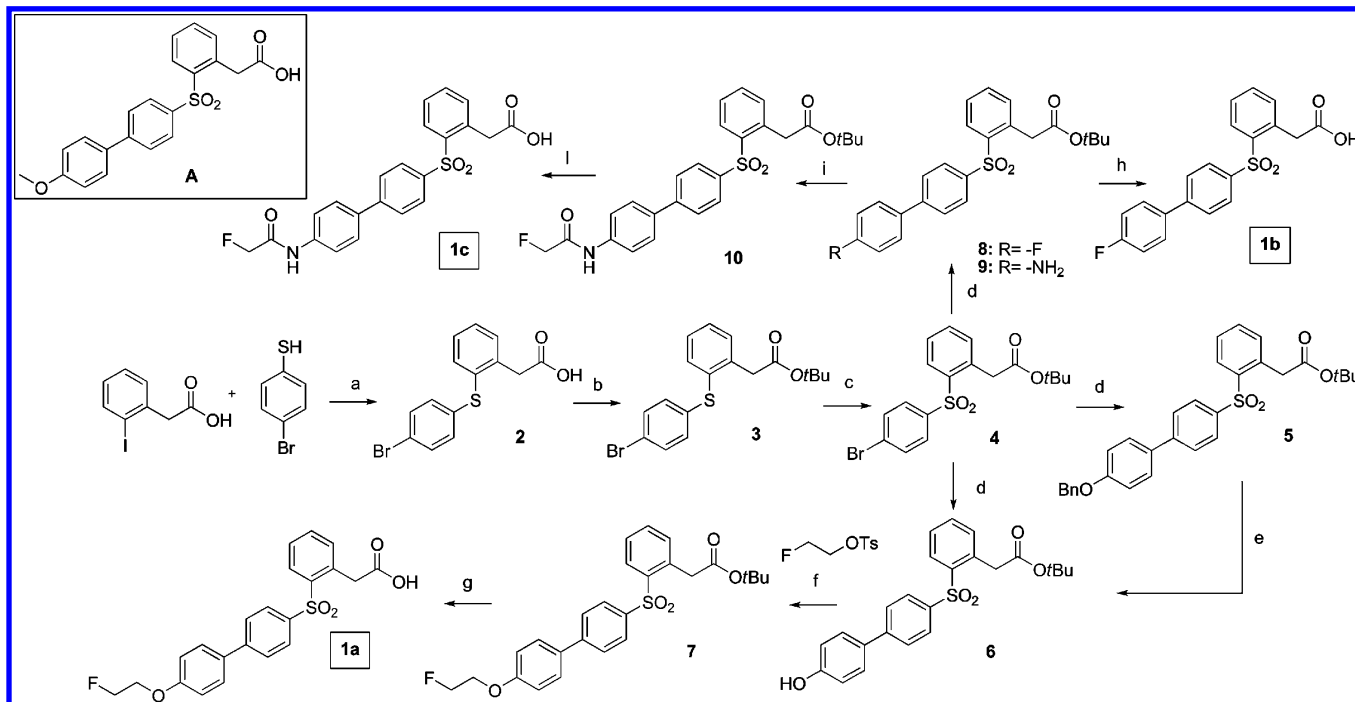
## **■** INTRODUCTION

Matrix metalloproteinases (MMPs) constitute a family of over 25 zinc- and calcium-dependent endopeptidases belonging to the superfamily of metzincines.<sup>1,2</sup> As with many other proteins of the extracellular matrix (ECM), MMPs are secreted or membrane-bound proteins with a complex multidomain structure. The primary role of each MMP is the degradation of specific structural components of the ECM, such as the different types of fibrillar collagen (the preferred substrate of MMP-1/8/13/18), nonfibrillar collagen (MMP-2/9) and proteoglycans (MMP-3/7/10).<sup>3</sup> In addition, MMPs have several other regulatory functions, including the processing of tissue-specific bioactive molecules, such as chemokines, cytokines, growth factors, and even other MMPs and their tissue inhibitors (TIMPs).<sup>4</sup> All together, MMPs have a pivotal role in tissue remodeling in normal conditions (angiogenesis, tissue repair, wound healing) as well as pathological states such

as cancer, inflammation, and neurodegeneration. In oncology, the role of MMPs has long been studied and debated, and it is nowadays well-established that certain members of this family, most notably gelatinase A (MMP-2), can sustain all stages of tumor progression, including proliferation, migration, angiogenesis, invasion, and metastasis.<sup>3,5,6</sup> In general, the relative level of each individual MMP increases with increasing tumor stage and is higher in malignant cancers than in normal or premalignant tissues, with maximum activity occurring at the tumor–stroma interface in areas of active invasion.<sup>7,8</sup> On the other hand, there is emerging evidence that some other metalloproteinases like MMP-3, MMP-8, and MMP-26 seem to have antitumor properties and to be linked with protective functions.<sup>9–11</sup> The specific role of each MMP in tumorigenesis

**Received:** February 1, 2013

**Published:** March 4, 2013

Scheme 1. Synthesis of Compounds 1a, 1b, and 1c<sup>a</sup>

<sup>a</sup>Reagents and conditions: (a) KOH, Cu, H<sub>2</sub>O, MW. (b) *N,N*-Dimethylformamide di-*tert*-butylacetal, toluene, 90 °C. (c) Oxone, THF, MeOH, H<sub>2</sub>O. (d) 4-Hydroxy-phenylboronic acid (**6**), 4-(benzyloxy)phenylboronic acid (**5**), 4-fluorophenylboronic acid (**8**), or 4-amino-phenylboronic acid hydrochloride (**9**), Pd(PPh<sub>3</sub>)<sub>4</sub>, K<sub>3</sub>PO<sub>4</sub>, H<sub>2</sub>O, dioxane, 85 °C. (e) H<sub>2</sub>, Pd/C 10%, MeOH, AcOH. (f) K<sub>2</sub>CO<sub>3</sub>, CH<sub>3</sub>CN, 82 °C. (g) TFA, DCM, 0 °C. (h) TFA, DCM, 0 °C. (i) Fluoroacetyl chloride, DIPEA, DMF. (l) TFA, DCM, 0 °C.

and their extracellular localization makes these enzymes attractive candidates not only as targets for therapeutics<sup>12,13</sup> but also as biomarkers for the grading of cancers. Assessment of the activity of a specific subset of MMPs in the tumor microenvironment by clinically relevant imaging techniques (e.g., MRI, nuclear medicine, etc) would therefore be of great potential for the choice, calibration, and assessment of the efficacy of therapy.<sup>14,15</sup>

Due to their high sensitivity, nuclear medicine imaging techniques such as single photon emission computed tomography (SPECT) and positron emission tomography (PET)<sup>14,16</sup> are well-amenable to true molecular or metabolic imaging applications and are currently exploited in oncology protocols for imaging of receptors, assessment of amino acid uptake, and glucose metabolism.<sup>17–19</sup> To obtain molecular images of MMPs, a number of broad-spectrum MMP inhibitors (MMPi) have been labeled with nuclides for either PET or SPECT imaging modality.<sup>14,20</sup> Most of the MMPi are based on the sulfonamido scaffold featuring a hydrophobic portion that inserts into the S<sub>1</sub>' specificity pocket of the enzyme and a metal chelating moiety (the zinc binding group, ZBG) that blocks the enzyme by chelating the Zn(II) ion within the active site. Two inhibitors belonging to this class, namely, CGS 27023A and its close analogue CGS 25966, have been labeled with a variety of radionuclides, including <sup>123</sup>I/<sup>125</sup>I for SPECT<sup>21</sup> and <sup>11</sup>C or <sup>18</sup>F for PET.<sup>22–24</sup> Despite *in vitro* studies or studies aimed at the visualization of nontumor vascular lesions that were promising, those tracers evaluated for the *in vivo* visualization of tumors gave contrasting results, as nonspecific uptake or binding were often found.<sup>14,25</sup> Furumoto and co-workers<sup>26</sup> introduced the alkynyl carboxylate [<sup>18</sup>F]SAV03 and its methyl ester [<sup>18</sup>F]SAV03 M prodrug, the latter showing a tumor

accumulation of radioactivity suitable for tumor visualization by PET. More recently, non-sulfonamido <sup>18</sup>F-labeled compounds have appeared, such as the [<sup>18</sup>F]aryltrifluoroborate analogue of marimastat, a peptidomimetic broad-spectrum MMPi.<sup>27</sup> The latter compound was evaluated on a well-characterized murine model of mammary carcinoma *in vivo*, and a low but detectable and specific uptake of the radiotracer was observed.

Some studies highlighted that the use of broad-spectrum inhibitors can have shortcomings in the correct interpretation of positive imaging results, as the uptake cannot be unambiguously related to increased activity of specific subsets of MMPs.<sup>25</sup> Therefore, the development of inhibitors endowed with enhanced selectivity toward MMP subsets might be highly beneficial for diagnostic imaging. The selectivity of inhibitors can be enhanced, though often at the expense of potency, by substituting the largely used hydroxamate for carboxylate or other weaker Zn(II) chelators.<sup>28</sup> The use of non-hydroxamate inhibitors can be advantageous in other aspects, since hydroxamates are known to be metabolically unstable and can interfere with other enzymes whose function is dependent on transition metal ions. A recent example of non-hydroxamate PET agents was reported by Breyholz et al.,<sup>29</sup> where pyrimidine-2,4,6-trione-based inhibitors with reduced lipophilicity have been radiolabeled with <sup>18</sup>F and biodistribution in mouse was evaluated.

In this work we present three new fluorinated arylsulfonate carboxylate inhibitors of MMPs and the radiochemistry used to obtain <sup>18</sup>F-labeled PET imaging agents. On the basis of previous promising results<sup>30</sup> obtained with phenylacetic carboxylates designed to selectively inhibit MMP-12, we have selected and suitably modified the scaffold A (Scheme 1). This

Table 1. IC<sub>50</sub> of Nonradioactive Fluorinated MMP Inhibitors against a Panel of MMPs and clogD Values

compd	IC <sub>50</sub> <sup>a</sup> (nM)							clogP <sup>b</sup>	clogD <sup>b</sup>
	MMP-1	MMP-2	MMP-3	MMP-9	MMP-12	MMP-13	MMP-14		
A <sup>c</sup>	4400 ± 330	47 ± 3.4	7500 ± 750	730 ± 58	140 ± 22	78 ± 9.7	740 ± 58	4.44	1.35
1a	18500 ± 1400	16 ± 1.9	7100 ± 530	107 ± 18	44 ± 2.7	22 ± 1.7	1600 ± 170	4.55	1.46
1b	11500 ± 550	230 ± 15	67000 ± 5100	3600 ± 490	400 ± 22	386 ± 37	4800 ± 460	4.63	1.54
1c	6100 ± 1400	61 ± 8	6800 ± 1000	1500 ± 83	500 ± 79	220 ± 15	4600 ± 1000	3.76	0.67

<sup>a</sup>Values are the mean ± SD of three experiments. <sup>b</sup>clogD represents the clogP of the compound at physiological pH, taking into account charged species. Values were calculated by the MOE (Molecular Operating Environment, CCG) software package. <sup>c</sup>Taken from ref 30.

compound has been chosen for its good activity toward MMP-2 and selectivity over MMP-1, compared to the other carboxylates developed in that study. We have decided to insert the fluorine atom in the para position on the biphenylsulfone group on the basis of synthetic feasibility and data taken from literature. Moreover, it was already known<sup>31,32</sup> that an elongation in that position (P1' substituent) could cause an increase of activity toward MMP-2 and a drop of activity for MMP-1. A selectivity over MMP-1 has been highly sought because this enzyme, together with MMP-14, has been hypothesized to cause the musculoskeletal syndrome (MSS) observed clinically with broad-spectrum inhibitors after long-term application.<sup>33</sup> Thus, fluorinated compounds **1a**, **1b**, and **1c** (Scheme 1) have been synthesized, their IC<sub>50</sub> values assessed in vitro with recombinant human MMPs, and radiolabeled with <sup>18</sup>F. A preliminary biodistribution of two of these radiotracers has been carried out in healthy athymic mice. Then the ability of the most promising tracer to label tumors in the murine U-87 MG glioblastoma model has been assessed and the specificity of tumor labeling evaluated.

## RESULTS

**Chemistry.** The O-ethylfluorinated carboxylate **1a** has been synthesized as described in Scheme 1. Thioether **2** was obtained through a microwave-assisted Cu-catalyzed Ullmann-type reaction as earlier reported in a precedent work of ours.<sup>30</sup> The carboxylate was then protected as *tert*-butyl ester via reaction with *N,N*-dimethylformamide di-*tert*-butyl acetal in toluene, yielding compound **3**, which was oxidized into sulfone **4** with oxone in a mixture of methanol, THF, and water. Arylsulfone **4** was then submitted to a palladium-catalyzed cross-coupling reaction (Suzuki conditions) with 4-hydroxyphenylboronic acid to give 4'-hydroxybiphenyl arylsulfone **6**. In order to improve the yield of this reaction and to overcome the troubles related to purification due to the presence of the highly reactive hydroxyl group, we alternatively synthesized the O-benzyl-protected biphenyl intermediate **5**, which was in turn converted into compound **6** by Pd/C-catalyzed hydrogenation. A substitution reaction of phenol **6** with 1-fluoro-2-tosyloxyethane in acetonitrile and K<sub>2</sub>CO<sub>3</sub> as base yielded the fluorinated-tailed *tert*-butyl ester **7**, which was converted into the carboxylic acid **1a** by deprotection with trifluoroacetic acid (TFA) in dichloromethane at 0 °C.

The synthesis of arylfluorinated carboxylate **1b** and fluorinated amide **1c** is also described in Scheme 1. 4-Bromoarylsulfone intermediate **4** was submitted to Suzuki coupling with 4-fluorophenylboronic acid or 4-aminophenylboronic acid, yielding respectively 4'-fluorinated ester **8** or 4'-amino ester **9**. Acid cleavage of compound **8** with TFA gave the corresponding carboxylate **1b**, while acetylation of **9** with fluoroacetyl chloride in the presence of *N,N*-diisopropylethyl-

amine (DIPEA) led to acetamido derivative **10**, which was in turn converted into carboxylate **1c** by acid hydrolysis.

**Inhibition of Matrix Metalloproteinases.** The final carboxylic acids were tested in vitro, with a fluorometric assay on purified enzymes, for their ability to inhibit MMPs (Table 1; see Table S1 in Supporting Information for values reported as inhibitor constant *K<sub>i</sub>*). Inhibitor A was used as a reference compound. As can be seen from the data reported in Table 1, the substitution of the *p*-methoxy group with a 2-fluoroethoxy group in **1a** caused an increase in activity for MMP-2/9/12/13 compared to the reference compound. Namely, **1a** showed an IC<sub>50</sub> of 16 nM on MMP-2 (three times more potent than parent A) and an IC<sub>50</sub> of 107 nM on MMP-9 (seven times more potent than A). These are very good potency data considering the carboxylate nature of the ZBG. Moreover, this increased activity for deep S1' pocket MMPs<sup>34</sup> like MMP-2/9/12/13 was accompanied by a drop of activity for MMP-1 and -14, whose inhibition was deemed to be responsible for MSS, and for MMP-3, considered as an antitarget in cancer therapy. Compounds **1b** and **1c**, bearing a fluorine atom and a 2-fluoroacetamido group in the para position on the biphenyl-sulfone moiety, respectively, showed a reduction in activity for all MMPs tested with respect to A. This effect was more marked with **1b**, which had an IC<sub>50</sub> of 230 nM on MMP-2 and 3600 nM on MMP-9. Compound **1c**, even if less active than A and **1a** on MMP-2 (IC<sub>50</sub> = 61 nM), presented a strong selectivity for this enzyme over all other tested MMPs.

Overall, **1a** showed the best characteristics of activity and selectivity to be used as a probe in the glioblastoma tumor model. In fact, this compound, with nanomolar activity for MMP-2/9 and marked selectivity over MMP-1/3/14, should be able to bind tightly, but not covalently, to MMP-2/9 that are overexpressed in the U-87 MG human glioblastoma cell line.<sup>35,36</sup> The concomitant inhibition of MMP-12 and MMP-13 should be beneficial, because also these enzymes have been recently found to be highly expressed in U-87 MG glioblastoma.<sup>37</sup>

**Interaction with Serum Albumin.** The binding affinities of **1a** and **1c** to human serum albumin (HSA) have been assessed by <sup>19</sup>F NMR titration of 1.0 mM solutions of the inhibitors with HSA. A progressive downfield shift with line broadening of the <sup>19</sup>F NMR signal is observed up to a protein:ligand ratio of 0.4:1 (from −147.7 ppm to a limiting value of −146.9 ppm; signal A, Figure 1), and then a new broad <sup>19</sup>F NMR signal emerges from the noise at −146.3 ppm (signal B) and becomes more intense than signal A at higher protein:ligand ratios. This can be explained by considering multiple binding sites on albumin. Although the appearance of two peaks due to the albumin-bound ligand hampers a rigorous quantitative analysis of the titration curve, a rough estimation of the dissociation constant for the lower affinity site (site A) could still be obtained by computer fitting of the <sup>19</sup>F NMR



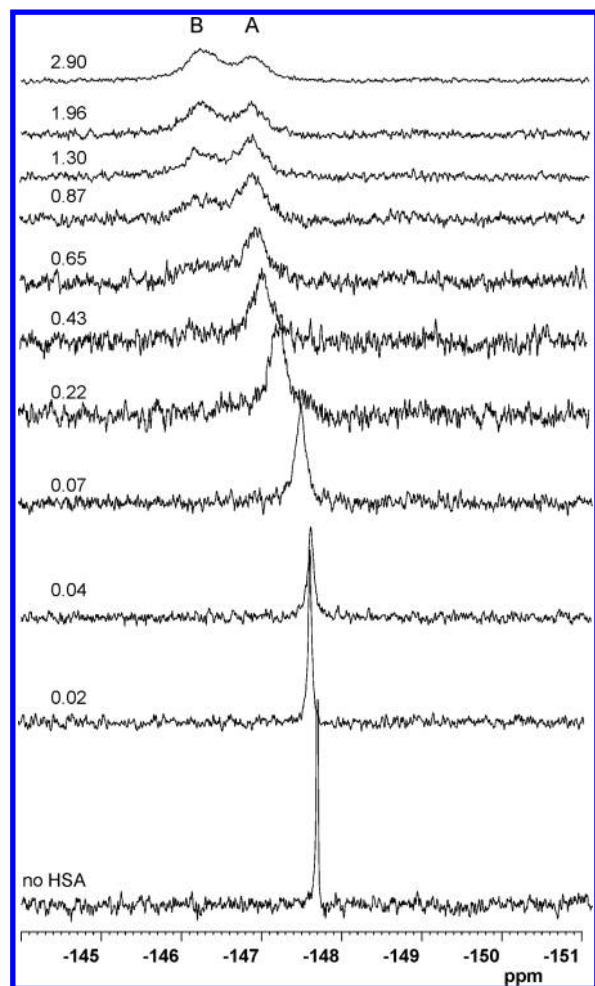


**Figure 1.**  $^{19}\text{F}$  NMR spectra of **1a** [1.0 mM, phosphate-buffered saline (PBS), pH 7.4] with increasing concentrations of defatted human serum albumin (HSA). The concentration of protein is given on the left as millimoles per liter.

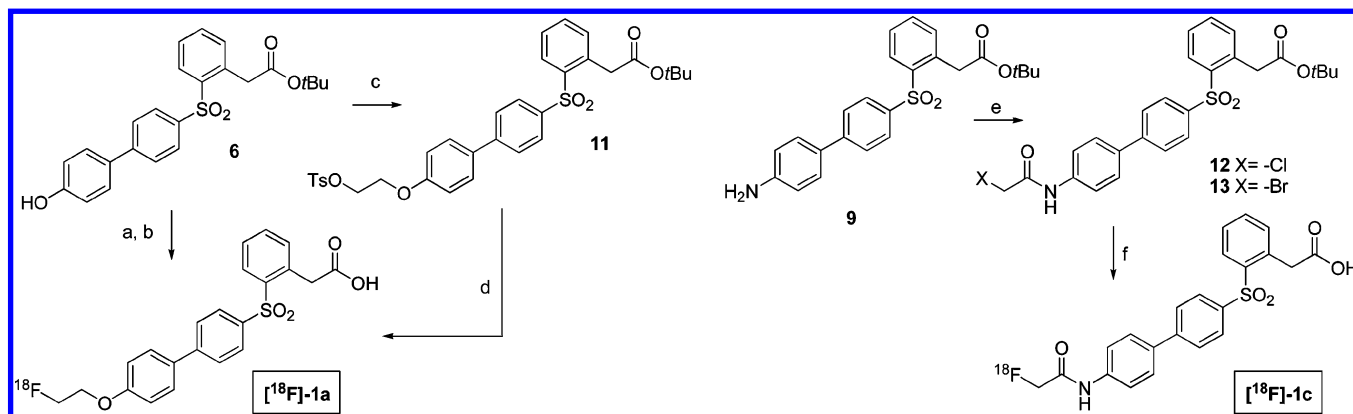
titration curve according to a model in which each albumin molecule is treated as having  $n$  independent binding sites.<sup>38</sup> An acceptable fitting could be obtained only by allowing  $n = 3$  (i.e., three equivalent binding sites per albumin molecule), each

having a dissociation constant  $K_d$  on the order of  $140\ \mu\text{M}$ . Thus, there are multiple equivalent lower affinity binding sites for **1a** on albumin (site A), and at least one binding site endowed with a higher affinity (site B). The  $^{19}\text{F}$  NMR titration of **1c** with albumin gave similar results, with the ligand distributing between one lower affinity ( $K_d$  on the order of  $10\ \mu\text{M}$ ) and one higher affinity binding site. These affinities for albumin are on the order of magnitude expected for organic anions containing a biphenyl moiety.<sup>39,40</sup> On this basis it can be foreseen that, in blood, a significant fraction of the tracers will be in the form of albumin complexes, resulting in prolonged in vivo half-life but also decreased availability for MMP binding and inhibition.

**Radiosynthesis.** The radiosynthesis of  $^{18}\text{F}$ -**1a** is shown in Scheme 2. As a first attempt, a two-step procedure was evaluated. The  $^{18}\text{F}$  was previously introduced by nucleophilic substitution on the ethylene glycol ditosylate and the resulting 1- $^{18}\text{F}$ fluoro-2-tosyloxyethane was reacted with the intermediate **6** to give  $^{18}\text{F}$ -**7** by nucleophilic substitution in the presence of sodium methoxide as base. This procedure provided a crude mixture in which the *tert*-butyl-protected compound  $^{18}\text{F}$ -**7** accounted only for 10% of the total radioactivity, whereas the main product likely resulted from nucleophilic substitution of the methoxide ion on 1- $^{18}\text{F}$ fluoro-2-tosyloxyethane. NaH and  $\text{K}_2\text{CO}_3$  were also tested instead of methoxide, but they were not able to provide better yields. The poor yield of the *tert*-butyl-protected intermediate  $^{18}\text{F}$ -**7**, which should be further deprotected and finally purified, prompted us to devise an alternative route for the radiosynthesis of  $^{18}\text{F}$ -**1a**. To improve the effectiveness and speed up the reaction time, the radiosynthesis of  $^{18}\text{F}$ -**1a** was reduced to a one-step procedure starting from tosyl intermediate **11**, synthesized by treatment of phenol **6** with an excess of glycol ditosylate<sup>41</sup> and potassium carbonate. Direct nucleophilic substitution of tosylate provided, after acidic removal of the *tert*-butyl protective group, compound  $^{18}\text{F}$ -**1a** with a moderate overall radiochemical yield (RCY) ( $10\% \pm 4\%$ , n.d.c.) but radiochemical purity as high as  $98\% \pm 2\%$ , within a total synthesis time of 70 min. Specific activity (end of synthesis, EOS) was  $5\ \text{GBq}/\mu\text{mol}$ .

For the radiosynthesis of  $^{18}\text{F}$ -**1c**, both chloro derivative **12** and bromo derivative **13** were prepared by acetylation of the 4-

**Scheme 2.** Radiosynthesis of Tracers  $^{18}\text{F}$ -**1a** and  $^{18}\text{F}$ -**1c**<sup>a</sup>



<sup>a</sup>Reagents and conditions: (a)  $(1)\ \text{C}_2\text{H}_4(\text{OTs})_2$ ,  $^{18}\text{F}[\text{K}(\text{K } 222)\text{F}]$ ,  $100\ ^\circ\text{C}$ ; (2)  $\text{MeONa}$ ,  $120\ ^\circ\text{C}$ . (b)  $\text{TFA}$ ,  $\text{CH}_3\text{CN}$ , rt. (c)  $\text{C}_2\text{H}_4(\text{OTs})_2$ ,  $\text{K}_2\text{CO}_3$ ,  $\text{CH}_3\text{CN}$ ,  $82\ ^\circ\text{C}$ . (d) (1)  $^{18}\text{F}[\text{K}(\text{K } 222)\text{F}]$ ,  $105\ ^\circ\text{C}$ ; (2)  $\text{TFA}$ ,  $\text{CH}_3\text{CN}$ , rt. (e) Chloroacetylchloride or bromoacetyl bromide, DIPEA, DMF. (f) (1)  $^{18}\text{F}[\text{K}(\text{K } 222)\text{F}]$ ,  $130\ ^\circ\text{C}$ ; (2)  $\text{TFA}$ ,  $\text{CH}_3\text{CN}$ , rt.

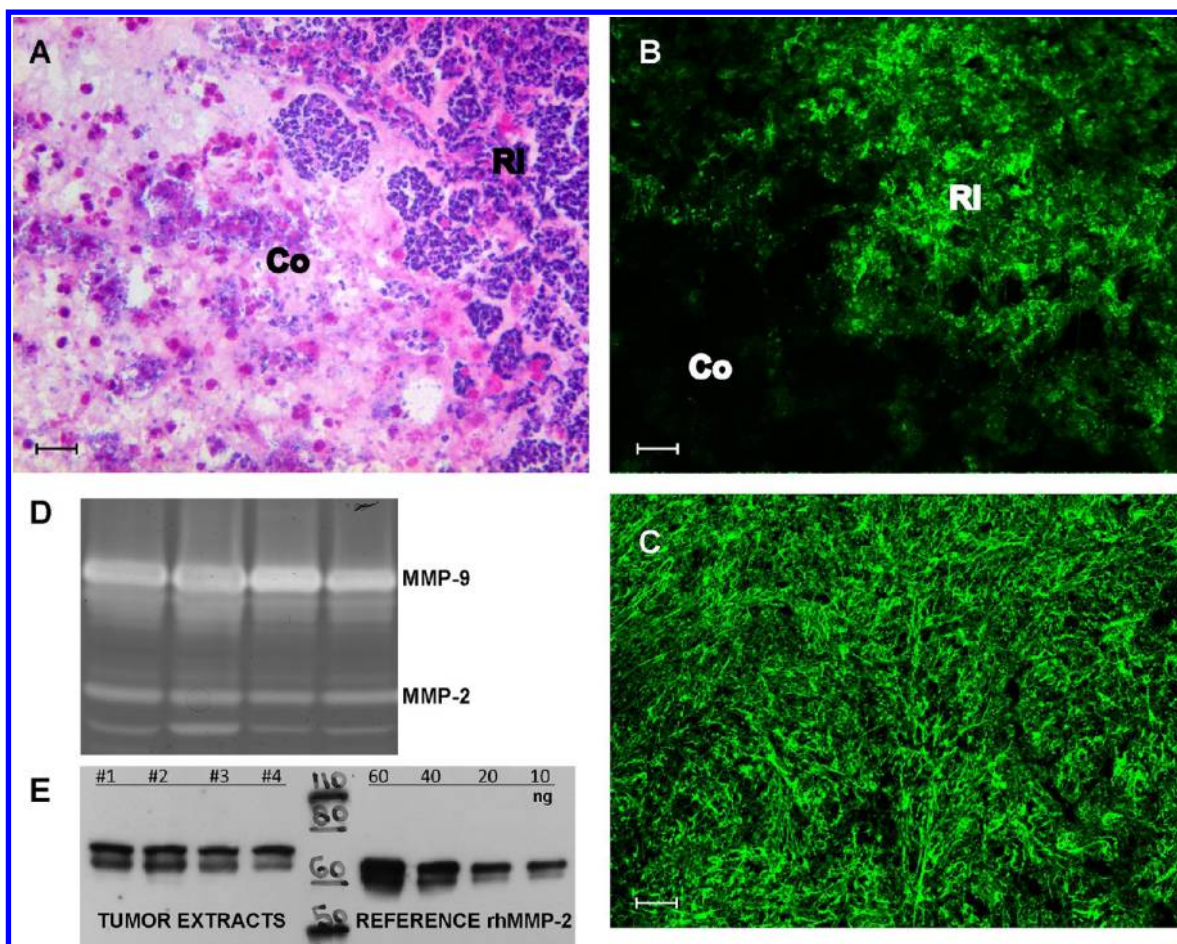


**Figure 2.** (A) Section of U-87 MG tumor stained with hematoxylin/eosin taken across the boundary between the tumor core (Co) and the tumor rim (Ri). Scale bar 54.6  $\mu\text{m}$ . (B) In situ DQ-gelatin zymography of a tumor section adjacent to that shown in panel A. Gelatinolytic activity by confocal fluorescence microscopy appears as green fluorescence on a black background. Scale bar 54.6  $\mu\text{m}$ . (C) In situ DQ-gelatin zymography of a tumor section taken across a high cellularity tumor region, showing diffuse gelatinase activity. Scale bar 54.6  $\mu\text{m}$ . (D) Gelatin zymography of U-87 MG tumor homogenates. Tumors were excised from mice within 12 h after [ $^{18}\text{F}$ ]-1a PET scans. Results from four individuals are shown. (E) Western blot assay for MMP-2. The lanes on the left are from four tumor extracts seeded at 20  $\mu\text{g}$  of protein. Bands of active MMP-2 and proMMP-2 are visible. The lanes on the right are relative to true rhMMP-2 (active form) used to build a calibration curve, seeded at 10–60 ng of MMP-2.

aminoarylsulfone **9** with chloroacetyl chloride or bromoacetyl bromide, respectively, in *N,N*-dimethylformamids (DMF) with DIPEA as the base. Only the chloro precursor **12** proved effective in providing *tert*-butyl-protected [ $^{18}\text{F}$ ]-**1c** by nucleophilic substitution of the halogen atom (Scheme 2). Following deprotection in acidic conditions, [ $^{18}\text{F}$ ]-**1c** was obtained with a RCY of  $3\% \pm 1\%$  (n.d.c) and radiochemical purity of 100%, within a total synthesis time of 60 min. Specific activity (EOS) was 12 GBq/ $\mu\text{mol}$ .

**Biological Characterization of Matrix Metalloproteinase Activity in Tumor Xenografts and Assessment of Target Site Density.** Gelatin zymography of whole tumor extracts (resection done within 12 h after PET scans,  $n = 4$ ) confirmed that, at the time of PET scans, the levels of MMP-2 and MMP-9 were high (Figure 2D), with MMP-9 gelatinolytic bands being more intense than those of MMP-2. To assess the distribution of gelatinase activity within the tumor mass, unfixed frozen xenografts ( $n = 6$ ) were excised and serial cryosections (10  $\mu\text{m}$  thick) were subjected in parallel to hematoxylin/eosin (HE) staining or in situ zymography with dye-quenched (DQ) gelatin (Figure 2A–C). HE sections clearly showed that U-87 MG xenografted tumors are typically composed by a necrotic core with visible cell debris and an

external rim with high cellularity. In situ zymograms made on adjacent slices showed that the MMP activity is uniformly distributed in the extracellular space within the high cellularity tumor periphery, whereas it is almost completely absent in the necrotic core. It is worth emphasizing that in situ zymography detects MMP-2 and MMP-9 in the active form only. However, minor contributions from other MMP members (for instance, collagenases) cannot be excluded.<sup>42</sup> Fluorescence arising from the breakdown of DQ gelatin was almost completely abolished by treating the tumor slices with MMP inhibitors such as ethylenediaminetetraacetic acid (EDTA) or 1,10-phenanthroline, indicating that endoproteases other than MMPs give a negligible fluorescence background (data not shown).

As zymographic techniques are hardly amenable to quantitative analysis, the assessment of target site density in tissue ( $B_{\text{max}}$ ) was accomplished by Western blotting (Figure 2E). MMP-2 has been chosen for quantification because the radiotracer [ $^{18}\text{F}$ ]-**1a** showed the maximum binding affinity for this member of the MMP family ( $K_d = 15$  nM; see Table S1 in Supporting Information). As available antibodies cannot distinguish between the zymogen and active form, MMP-2 appeared as two resolved bands centered at a MW of about 70 kDa, corresponding to the zymogen (high MW) and the active



form (low MW). A calibration curve has been built by running standard rhMMP-2 (active form) in the same gel, within a loading range of 10–60 ng. The densitometric response was linear within this range. Densitometric readings of tumor extracts ( $n = 4$ ) were converted into nanograms of MMP2 per microgram of protein by means of such a calibration curve. Whole tumor extracts yielded a total concentration of MMP-2 of  $1.5 \pm 0.3$  ng of MMP2/ $\mu$ g of protein, corresponding to 0.021 nmol of MMP2/mg of protein. This value refers to total MMP-2 in whole tumor extracts, that is, the cumulative concentration of zymogen and active forms. This can be converted to concentration in the whole tumor by considering that 1 fmol of MMP2/mg of protein corresponds to 0.1 nM concentration,<sup>43</sup> yielding a total MMP-2 concentration of 2.1  $\mu$ M. The ratio between the densitometric reading of active MMP-2 against total MMP-2 revealed that  $34\% \pm 13\%$  of total MMP-2 (corresponding to a tissue concentration of 0.7  $\mu$ M) is in the active form. However, active MMP-2 as far as detected by Western blotting is contributed by truly active MMP-2 and MMP-2 whose activity was inhibited by TIMPs in tissue (sodium dodecyl sulfate–polyacrylamide gel electrophoresis, SDS–PAGE, dissociates those inhibition complexes and does not allow us to distinguish between inhibited and noninhibited forms). Therefore, a tissue concentration of 0.7  $\mu$ M would be an overestimation of the accessible site density. Literature data indicates that 6–15% of MMP-2 is in the active form in glioblastomas.<sup>44</sup> Studies on the levels of circulating MMP-2 in blood (i.e., substantially released from tumor bearing sites) show that activated forms are about 10% of total MMPs.<sup>45</sup> For an average value of 10%, the active MMP-2 in tissue (i.e., the target site density  $B_{\max}$ ) will be 210 nM (average over the whole tumor mass). A receptor binding potential ( $B_{\max}/K_d$ ) of 14.1 can be eventually obtained, which is encouraging for imaging purposes.<sup>46</sup> This value must be regarded as a lower limit. The actual value in the tumor rim could be higher, if it is considered that (i)  $B_{\max}$  has been calculated as the average for the whole tumor mass, while in situ zymograms clearly showed accumulation of active MMP-2 within the tumor periphery; (ii) this calculation does not take into account MMPs other than MMP-2, which can also contribute to  $B_{\max}$ ; and (iii) recovery of MMP-2 by the mild tissue extraction procedure we employed is likely incomplete.<sup>47</sup>

**Biodistribution and Tumor Uptake: Initial Small Animal Studies.** For biodistribution studies, 6–8 week old healthy CD1 nude mice were intravenously injected with a typical dose of 7.4 MBq of [ $^{18}$ F]-1a ( $n = 3$ ) or its *tert*-butyl ester [ $^{18}$ F]-7 ( $n = 2$ ) or [ $^{18}$ F]-1c ( $n = 2$ ). [ $^{18}$ F]-7 was included in biodistribution studies because it represents the pro-tracer form of [ $^{18}$ F]-1a and, by analogy with findings by Furumoto and co-workers,<sup>26,48</sup> it might be endowed with a better uptake in tumor and less accumulation in the liver compared with the active [ $^{18}$ F]-1a form. Dynamic PET scans were performed and images were reconstructed at several time points within a time window of 2.5 h. [ $^{18}$ F]-1a and [ $^{18}$ F]-1c showed similar pharmacokinetic profiles that are essentially characterized by fast uptake of radioactivity by the liver followed by delayed accumulation in the gut (Figure 3). A peak of activity in the liver is reached within 10 min postinjection (with maximum percentage injected dose per gram of tissue, % ID/g, of 11.2 and 11.0 for [ $^{18}$ F]-1a and [ $^{18}$ F]-1c, respectively), and then the radioactivity levels off at about 8.5% ID/g ([ $^{18}$ F]-1a) and 6.1% ID/g ([ $^{18}$ F]-1c) after 45 min. The radioactivity steadily accumulates in the duodenum and small intestine, from 2.5%

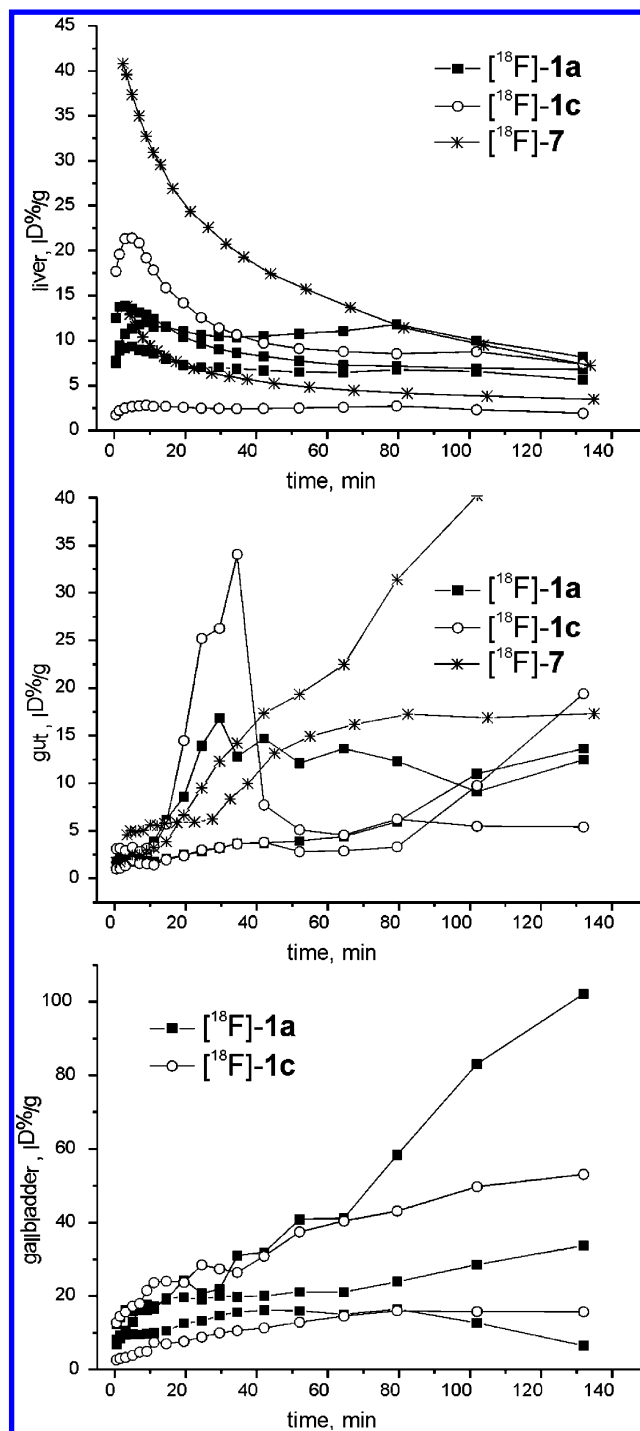


**Figure 3.** Biodistribution of (■) [ $^{18}$ F]-1a, (\*) [ $^{18}$ F]-7, and (○) [ $^{18}$ F]-1c in healthy nude mice. Time–activity curves for liver, gut, and gallbladder are shown.

ID/g (10 min, [ $^{18}$ F]-1a) and 2.4% ID/g (10 min, [ $^{18}$ F]-1c) to about 13.1 and 12.4% ID/g at 140 min postinjection. The increase of radioactivity in the small intestine appears to be linked with the decrease in the liver. Both [ $^{18}$ F]-1a and [ $^{18}$ F]-1c clearly show transit through the gallbladder, which emerges in images reconstructed at 30 min as a bright spot well-contrasted from surrounding hepatic tissues (Figure S1 in Supporting Information). [ $^{18}$ F]-7 shows approximately the same time–activity course as [ $^{18}$ F]-1a and [ $^{18}$ F]-1c, but the uptake in liver and gastrointestinal tract is higher (21.6% ID/g and 4.1% ID/g

after 10 min, respectively) and the uptake by the gallbladder cannot be clearly seen. For all tracers, time–activity curves suggest hepatobiliary clearance, which is in line with the hydrophobic nature of the tracers. A relationship between high radioactivity levels in the bile and uptake in the duodenum has been observed for other  $^{18}\text{F}$  radiotracers based on amphiphilic, sulfonamide-type MMP inhibitors.<sup>23,26</sup> Uptake of radioactivity in the head has been evaluated by static PET scans performed 2.5 h postinjection. Brain uptake was comparable to background (data not shown), indicating that the compound cannot cross the blood–brain barrier. No accumulation of radioactivity in the skeleton was observed, indicating that the tracers are metabolically stable toward defluorination and do not release [ $^{18}\text{F}$ ]fluoride.

Ligand [ $^{18}\text{F}$ ]-1a was selected to study the uptake of radioactivity in a human glioblastoma mouse model, as this ligand presents the best trade-off between the MMP inhibition profile and efficiency of radiosynthesis. No particular advantage, in terms of biodistribution, was observed by using its protracer form, [ $^{18}\text{F}$ ]-7. Human glioblastoma U-87 MG cells were subcutaneously injected in the left flank of 6-week-old athymic CD1 female nude mice. Tumors having a volume of about 200–300 mm<sup>3</sup> typically developed after 1 week. The time course of tumor uptake determined with dynamic PET scans (over a time span of 2.5 h) revealed that the radioactivity within the tumor reached a level of 1.1% ID/g at 10 min, leveling off at 1.7% ID/g at about 100 min postinjection (data not shown). On this basis, further PET images aimed at a more detailed assessment of [ $^{18}\text{F}$ ]-1a tumor uptake were performed in the static mode 100 min after tracer injection. This timing scheme was deemed to be an acceptable trade-off between accumulation of radioactivity into the tumor and minimization of background in neighboring regions (mainly due to the high uptake and retention of the tracer in the liver).

To confirm tumor localization and viability, glioblastoma-bearing mice ( $n = 5$ ) were subjected to a [ $^{18}\text{F}$ ]-1a PET scan sequentially followed by a [ $^{18}\text{F}$ ]FDG scan, as shown in Figure 4A. The uptake of [ $^{18}\text{F}$ ]-1a within the tumor was  $1.40\% \pm 0.15\%$  ID/g, approximately 3 times lower than that of [ $^{18}\text{F}$ ]FDG ( $4.39\% \pm 0.28\%$  ID/g). Tumors grown to a small volume ( $<200$  mm<sup>3</sup>) showed a uniform intratumor distribution of both [ $^{18}\text{F}$ ]-1a and [ $^{18}\text{F}$ ]FDG, whereas larger tumors (250–560 mm<sup>3</sup>) showed a preferential accumulation of tracers in the rim as compared to the core (a sample PET image is given in Figure 4A). Within larger tumors, [ $^{18}\text{F}$ ]-1a appeared to have a more marked accumulation within the rim as compared to [ $^{18}\text{F}$ ]FDG (Table S2 in Supporting Information).

To address the specificity of MMP targeting, a group of mice ( $n = 6$ ) was treated with the broad-spectrum MMP inhibitor ilomastat (also known as GM6001)<sup>49,50</sup> to saturate the MMPs active sites and make them unavailable to [ $^{18}\text{F}$ ]-1a ( $K_i$  of ilomastat toward MMPs is generally lower than that of [ $^{18}\text{F}$ ]-1a, as the ZBG of the former inhibitor is hydroxamate). The inhibitor was administered intraperitoneally at a dose of 40–160 mg/kg, 30 min before injection of [ $^{18}\text{F}$ ]-1a to allow it to enter the systemic circulation. PET images (Figure 4B) essentially revealed the same features found without blocking of MMPs with the cold inhibitor. The quantitative evaluation of percentage injected dose per gram of tissue (% ID/g) revealed a small but appreciable effect of preblocking MMPs on radioactivity uptake (Figure 5). The difference of [ $^{18}\text{F}$ ]-1a uptake in the tumor rim between preblocked and unblocked tumors was borderline statistically significant (Student's  $t$  test  $p$

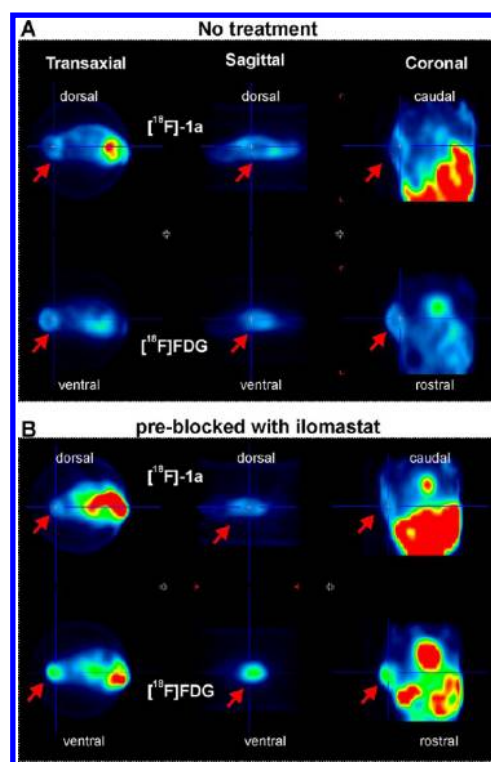


**Figure 4.**  $^{18}\text{F}$  PET images of the abdomen of nude mice subcutaneously grafted with a human U-87 MG glioblastoma. Red arrows show the tumor in different slices. (A) PET images obtained by sequential administration of [ $^{18}\text{F}$ ]-1a (upper row) and [ $^{18}\text{F}$ ]FDG (bottom row), showing colocalization of tracer uptake. The [ $^{18}\text{F}$ ]-1a scan was acquired 100 min post-tracer injection; [ $^{18}\text{F}$ ]FDG was injected immediately after completion of the [ $^{18}\text{F}$ ]-1a scan and the image was acquired 45 min post-[ $^{18}\text{F}$ ]FDG injection. Both scans were static acquisitions (injected dose 7.4 MBq, acquisition time 30 min). (B) PET images obtained by sequential administration of [ $^{18}\text{F}$ ]-1a (upper row) and [ $^{18}\text{F}$ ]FDG (bottom row), in a mouse that received 40 mg/kg of the broad-spectrum MMP inhibitor ilomastat 30 min before injection of [ $^{18}\text{F}$ ]-1a. The timing scheme and injected doses are the same as in panel A. Percentage injected dose per gram of tissue (% ID/g) values from these images are detailed in Table S2 in Supporting Information.

= 0.054). However, statistical significance was definitively achieved (Student's  $t$  test  $p = 0.014$ ) if the ratio between the uptake of [ $^{18}\text{F}$ ]-1a (tumor rim) and the uptake of [ $^{18}\text{F}$ ]FDG (whole tumor) was considered (in the following, such uptake ratio will be abbreviated as UR). This clearly indicates that the radioactivity of [ $^{18}\text{F}$ ]-1a in the tumor rim is due to a combination of specific (enhanced retention of [ $^{18}\text{F}$ ]-1a due to true binding to target MMPs) and aspecific contributions. The difference between the average uptake of [ $^{18}\text{F}$ ]-1a in preblocked/unblocked tumors was used to estimate the relative contributions of specific/aspecific uptake, yielding about 18% specific binding over total uptake.

## DISCUSSION

One of the advantages to using MMPs as a molecular target for an imaging agent is that these enzymes are secreted and activated in the extracellular environment, avoiding the need to transfer the radiolabeled probe to intracellular compartments.<sup>14</sup> However, there are also disadvantages linked to the large number of MMP family members that might obscure the detection of those members that are more descriptive of a



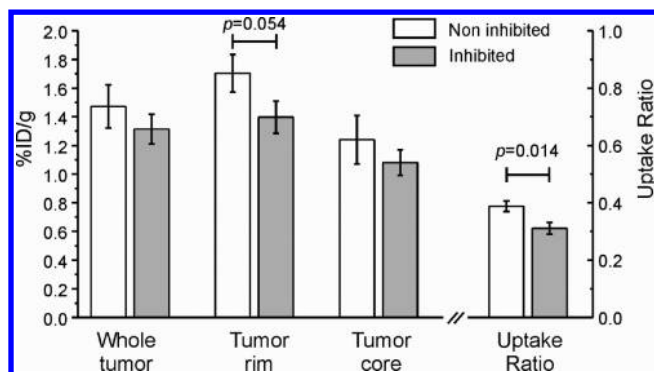


**Figure 5.** Average percentage injected dose per gram of tissue (% ID/g) measured in  $[^{18}\text{F}]\text{-1a}$  PET images in mice pretreated (gray columns) or not (white columns) with the broad-spectrum MMP inhibitor ilomastat (data listed in Table S2 in Supporting Information). (Left y-axis) Comparisons of the uptake of  $[^{18}\text{F}]\text{-1a}$  over the whole tumor, the tumor rim, or the tumor core. (Right y-axis) Comparison of the uptake ratio UR is shown. (UR is defined as the ratio between uptake of  $[^{18}\text{F}]\text{-1a}$  in the tumor rim and uptake of  $[^{18}\text{F}]\text{FDG}$  within the whole tumor; see text for details.) Error bars represent standard errors. Student's *t* test *p*-values are given where differences are statistically significant.

disease. Therefore, selectivity of the radiotracer for a subset of MMP members can be advantageous. Among the fluorinated arylsulfone MMP inhibitors we have presented, **1a** showed the best MMP affinity profile, being endowed with nanomolar activity for MMP-2/9/12/13 and a marked selectivity over MMP-1/3/14. To verify whether such affinity is sufficient for MMP imaging in our U-87 MG glioblastoma mouse model, we estimated  $B_{\text{max}}$  and  $B_{\text{max}}/K_d$  in the tumor. Under the hypothesis that active MMP-2 was the only target,  $B_{\text{max}}/K_d$  of 14.1 could be obtained. This is encouraging for imaging MMP activity with  $[^{18}\text{F}]\text{-1a}$ , because a  $B_{\text{max}}/K_d$  ratio  $\geq 10$  has been shown to be sufficient for imaging with radiotracers having nanomolar affinities.<sup>43,46</sup>

On the other hand, the biodistribution profiles of the tracers were dominated by high uptake/retention by the liver, predominance of hepatobiliary excretion, and strong interaction with albumin. These features are linked to the hydrophobic (**7**) or anionic, amphiphilic (**1a**, **1c**) chemical nature of our PET tracers. The hepatobiliary clearance route poses a serious limitation on the use of our tracers for imaging purposes, because it leads to high background radioactivity in the liver and gastrointestinal tract, which might obscure detection of nearby regions with true high MMP activity. This drawback is rather common to  $^{18}\text{F}$ -conjugated small-molecule MMP inhibitors and stems from the fact that hydrophobic groups are essential for the ligand to be conferred with a suitable MMP binding affinity and specificity.<sup>23,24,27</sup> Although there are some examples of improved biodistribution by lowering the overall log *D* of the tracer, for instance through insertion of small PEG chains at suitable positions, the effect on the ability of the resulting tracers to target MMPs *in vivo* has still to be assessed.<sup>29,51</sup>

Despite the nonoptimal biodistribution,  $[^{18}\text{F}]\text{-1a}$  showed detectable uptake in xenografted U-87 MG glioblastoma, reaching a level of 1.40% ID/g (whole tumor). The uptake levels of the compound tested were appreciably lower than those of  $[^{18}\text{F}]\text{FDG}$  (4.39% ID/g, whole tumor) but slightly larger or very similar with respect to those of other carboxylate-based small-molecule radiotracers targeted to MMPs.<sup>26,52</sup> PET

images of U-87 MG glioblastomas showed that  $[^{18}\text{F}]\text{-1a}$  localizes in the tumor rim more specifically than  $[^{18}\text{F}]\text{FDG}$  does. Such difference can be due to the very different physicochemical properties of  $[^{18}\text{F}]\text{-1a}$  (negatively charged, hydrophobic) as compared to  $[^{18}\text{F}]\text{FDG}$  (neutral, very hydrophilic), possibly affecting their diffusion within the tumor. However, the peripheral localization of  $[^{18}\text{F}]\text{-1a}$  is well consistent with the intratumor localization of MMP activity, as *in situ* zymography of U-87 xenografts showed that MMP activity is rather uniform in the extracellular space within the tumor rim (showing high cellularity), whereas it disappears within the necrotic core (Figure 2). This finding is in agreement with maximum gelatinase activity being typically found at the leading invasive edge of solid tumors.<sup>6–8</sup> However, it must also be considered that  $[^{18}\text{F}]\text{-1a}$  has a micromolar affinity for albumin binding, and because albumin is the most abundant serum protein (reaching a concentration of 35 mg/mL in mice), the tracer can be considered to be largely bound to albumin in blood. The albumin/radiotracer complex, either circulating within the neo-formed blood vessels or being retained through the EPR effect in the perivascular extracellular space, might be considered as the major aspecific source of radioactivity retention within the tumor rim.

Assessment of the specific-to-aspecific ratio of tracer accumulation has been done by comparing the uptake of  $[^{18}\text{F}]\text{-1a}$  with/without preblockage of MMP active sites by the cold, broad-spectrum MMP inhibitor ilomastat. A similar approach has been successfully used to assess the specificity of tumor labeling by other MMP-directed radiotracers, including a  $^{18}\text{F}$ -labeled version of the broad-spectrum MMP inhibitor marimastat.<sup>27,52</sup> Interestingly, we found a small but statistically significant difference in the uptake ratio (UR) between preblocked and unblocked tumors. The UR represents a normalization of the tumor uptake of the MMP-targeted tracer by the metabolic activity within the tumor itself, as far as evaluated by  $[^{18}\text{F}]\text{FDG}$  uptake. This normalization gives a better evaluation of the specific-to-aspecific ratio than the direct comparison between absolute tumor uptake (% ID/g) of the MMP-targeted tracer, essentially because the nonspecific uptake within a group of nonidentical tumors can be scaled out. The difference between average uptakes of  $[^{18}\text{F}]\text{-1a}$  in preblocked/unblocked tumors yields that as much as 18% of total uptake may be considered as specific. It is hard to discuss this result against those for analogous MMP-targeted tracers because, to the best of our knowledge, no other explicit figures are available from literature, and specificity of uptake has been treated mostly in a qualitative way. Indeed, a large number of MMP-targeted tracers studied in the past decade were deemed to give disappointing results *in vivo* because of insufficient uptake specificity.<sup>20,25</sup> In a recent work with marimastat labeled with  $^{18}\text{F}$  through nonconventional aryltrifluoroborate radiochemistry (Marimastat- $\text{ArBF}_3$ ), a high specificity of tumor uptake has been found. Although no explicit number is given, a specificity of 60–70% can be inferred from graphs reported therein.<sup>27</sup> A very recent work dealing with a fluorescent-labeled, hydroxamate MMP inhibitor (Cy5.5-AF489) yielded a specificity of about 30%.<sup>53</sup> Both Marimastat- $\text{ArBF}_3$  and Cy5.5-AF489 are very hydrophilic, hydroxamic-based compounds with inhibition potencies in the nanomolar range, suggesting that the more hydrophilic the tracers are, the more favorable the tumor uptake specificity is. However, care must be exercised in making more quantitative comparisons, as tumor

types, staging, and MMP expression profiles are widely different among these and our study.

## CONCLUSION

In conclusion, our  $^{18}\text{F}$ -labeled probe has the advantage of some selectivity toward a panel of MMPs, but the potential for imaging MMPs activity in vivo is strongly limited by the low specificity of tumor uptake and high uptake in the liver and gastrointestinal tract (GIT). This study also underlines that, besides optimization of the tracer hydrophobicity (log D) for better biodistribution, minimization of the affinity for serum albumin also has to be pursued to achieve highly efficient and specific tumor labeling. The latter aspect has never been considered in past studies. A very subtle balance of structural features is then required for an optimal balance between specificity toward selected MMP members, specificity of tumor uptake, and acceptable biodistribution. Functionalization of the arylsulfone scaffold at carefully selected positions with hydrophilic groups, such as mini-PEG chains,<sup>29</sup> or modification of the net charge of the molecule could be viable routes to achieve this.

## EXPERIMENTAL SECTION

**Synthesis of Precursors and  $^{19}\text{F}$ -Labeled Inhibitors: General Procedures.**  $^1\text{H}$ ,  $^{19}\text{F}$ , and  $^{13}\text{C}$  NMR spectra were determined with a JEOL ECP 400 ( $^1\text{H}$  at 400,  $^{13}\text{C}$  at 100 MHz) spectrometer or with a Bruker Avance III 500 MHz spectrometer ( $^1\text{H}$  at 500 MHz,  $^{13}\text{C}$  at 125 MHz,  $^{19}\text{F}$  at 470 MHz).  $^1\text{H}$  and  $^{13}\text{C}$  chemical shifts ( $\delta$ ) are reported in parts per million referenced to tetramethylsilane by using the residual signal of deuterated solvents as a secondary reference. Coupling constants  $J$  are reported in hertz (Hz).  $^{13}\text{C}$  NMR spectra were acquired with broadband proton decoupling.  $^{19}\text{F}$  chemical shifts were referenced to  $\text{CFCl}_3$  ( $\delta = 0$  ppm). The following abbreviations are used: singlet (s), doublet (d), triplet (t), double-doublet (dd), broad (br), and multiplet (m). Where indicated, the elemental compositions of the compounds agreed to within  $\pm 0.4\%$  of the calculated value. Chromatographic separations were performed on silica gel columns by flash column chromatography (Merck silica gel 60,  $230 \pm 400$  mesh) or by use of Isolute Flash Si II cartridges (Biotage). Reactions were followed by thin-layer chromatography (TLC) on Merck aluminum silica gel (5554) sheets that were visualized under a UV lamp (254 nm). Evaporation was performed in vacuo (rotating evaporator). Sodium sulfate was always used as the drying agent. Microwave-assisted reactions were run in a CEM Discover LabMate microwave synthesizer. Mass spectra with electrospray ionization (ESI) were recorded on a SQD 3100 mass detector (Waters), operating in positive- or negative-ion mode, with methanol as the carrier solvent. The purity of the final compounds was determined by reverse-phase HPLC on a 1525 Waters liquid chromatograph with a Waters Atlantis C18 column ( $150 \text{ mm} \times 4.6 \text{ mm}$ ,  $5 \mu\text{m}$ ); solvent A,  $\text{H}_2\text{O}/\text{TFA}$  0.1%; solvent B,  $\text{CH}_3\text{CN}/\text{TFA}$  0.1%; gradient of A from 40% to 80% in 18 min at a flow rate of 1 mL/min over a total run of 30 min (UV monitoring at the fixed wavelength of 254 nm). The purity of every compound synthesized was determined by the ratio of the integrated HPLC peak area for the compound of interest over the integrated HPLC peak area for all peaks. Purities were  $>95\%$  if not specified otherwise.

**2-[2-(4-Bromophenylthio)phenyl]acetic Acid (2).** A sealed tube containing 2-iodophenylacetic acid (1g, 3.82 mmol), 4-bromobenzenethiol (721.7 mg, 3.82 mmol), potassium hydroxide (427.8 mg, 7.64 mmol), copper powder (24.27 mg, 0.382 mmol), and water (1.9 mL) was submitted to microwave irradiation (two cycles of 6 min each at power 180 W,  $T_{\text{max}} = 140^\circ\text{C}$ , 100 psi); the sample was cooled during irradiation with a flow of compressed air. The obtained suspension was dissolved in a solution of 2 N KOH and then filtered. The filtrate was acidified with 1 N HCl, and the formed precipitate was filtered and

dried under reduced pressure ( $T = 50^\circ\text{C}$ ) to give a white precipitate (960 mg, 2.97 mmol, 77% yield).

**tert-Butyl 2-[2-(4-Bromophenylthio)phenyl]acetate (3).** A solution of the carboxylic acid 2 (2.2 g, 6.81 mmol) in dry toluene (13.07 mL) containing *N,N*-dimethylformamide di-*tert*-butyl acetal (4.70 mL, 27.23 mmol) was heated at  $95^\circ\text{C}$  while refluxing. After 3 h, toluene was evaporated and the product was purified by flash chromatography on silica gel (*n*-hexane/EtOAc 18:1) to afford a yellow oil (830 mg, 2.19 mmol, 32% yield).

**tert-Butyl 2-[2-(4-Bromophenylsulfonylethyl)phenyl]acetate (4).** To a stirred solution of sulfide 3 (800 mg, 2.109 mmol) in methanol (10.55 mL) and THF (31.64 mL) was added a solution of oxone [25 g, 42.18 mmol in water (42 mL)]. After 20 h of stirring, THF was evaporated in vacuo, the suspension was diluted with water, and the product was extracted with EtOAc. Organic phases were dried over  $\text{Na}_2\text{SO}_4$  and concentrated in vacuo to yield a white solid (990 mg, quantitative yield).

**General Procedure for Synthesis of Compounds 5 and 6.** To a stirred solution of arylbromide 4 (200 mg, 0.486 mmol) in water (1.07 mL) and dioxane (4.86 mL) under  $\text{N}_2$  atmosphere were added 4-hydroxyphenylboronic acid or 4-(benzyloxy)phenylboronic acid (0.535 mmol), potassium phosphate tribasic (340.45 mg, 1.604 mmol), and tetrakis(triphenylphosphine)palladium(0) (28 mg, 0.0243 mmol). The mixture was refluxed at  $85^\circ\text{C}$  under stirring for 5 h, and then the reaction was quenched with a saturated solution of  $\text{NaHCO}_3$  and the product was extracted with EtOAc. Organic phases were then washed with water and brine, dried over  $\text{Na}_2\text{SO}_4$ , and concentrated in vacuo.

**tert-Butyl 2-[2-[4'-(Benzyloxy)biphenyl-4-ylsulfonylethyl]phenyl]acetate (5).** The crude product was purified by flash chromatography on silica gel (*n*-hexane/EtOAc 8:1) by use of an Isolute Si II cartridge (Biotage) to afford a white solid (43% yield).

**tert-Butyl 2-[2-(4'-Hydroxybiphenyl-4-ylsulfonylethyl)phenyl]acetate (6).** The title compound obtained from intermediate 4 was purified by flash chromatography on silica gel (*n*-hexane/EtOAc 4:1) by use of an Isolute Si II cartridge (Biotage) to give a light brown oil (24% yield). Alternatively, a solution of compound 5 (0.758 mmol) in MeOH (54.3 mL) was stirred under hydrogen atmosphere in the presence of 10% Pd-C (1:2 w/w) and glacial acetic acid (54.3 mL) for 17 h at room temperature. The resulting mixture was filtered on Celite and the filtrate was evaporated under reduced pressure to afford a yellow oil (70% yield).

**tert-Butyl 2-[2-[4'-(2-Fluoroethoxy)biphenyl-4-ylsulfonylethyl]phenyl]acetate (7).** A suspension of phenol 6 (33 mg, 0.078 mmol), 1-fluoro-2-tosyloxyethane (22.07 mg, 0.1 mmol), and potassium carbonate (21.57 mg, 0.156 mmol) in  $\text{CH}_3\text{CN}$  (1 mL) was refluxed overnight under nitrogen atmosphere. The mixture was diluted with EtOAc and washed with water. EtOAc was dried over  $\text{Na}_2\text{SO}_4$  and concentrated in vacuo to yield a yellow oil (29 mg, 0.06 mmol, 80% yield).

**2-[2-[4'-(2-Fluoroethoxy)biphenyl-4-ylsulfonylethyl]phenyl]acetic acid (1a).** To a  $0^\circ\text{C}$  solution of *tert*-butyl ester 7 in dry  $\text{CH}_2\text{Cl}_2$  was added dropwise trifluoroacetic acid. The reaction was stirred at  $0^\circ\text{C}$  for 5 h and then TFA was evaporated. The crude product was purified by trituration with  $\text{Et}_2\text{O}$  and *n*-hexane to afford a light pink solid (16.4 mg, 0.04 mmol, 64% yield).  $^1\text{H}$  NMR (acetone- $d_6$ )  $\delta$  4.07 (s, 2H); 4.33 (m,  $^2J_{\text{H-H}} = 4.03$  Hz,  $^3J_{\text{H-F}} = 29.29$  Hz, 2H); 4.79 (m,  $^2J_{\text{H-H}} = 4.03$  Hz,  $^3J_{\text{H-F}} = 47.60$  Hz, 2H); 7.09 (d,  $J = 8.79$  Hz, 2H); 7.47–7.49 (m, 1H); 7.56–7.60 (m, 1H); 7.63–7.71 (m, 1H); 7.68 (d,  $J = 7.89$  Hz, 2H); 7.83 (d,  $J = 8.79$  Hz, 2H); 7.94 (d,  $J = 8.79$  Hz, 2H); 8.17–8.19 (m, 1H).  $^{13}\text{C}$  NMR (acetone- $d_6$ )  $\delta$  37.61, 67.42, 67.62, 81.24, 82.92, 115.20, 127.19, 128.02, 128.19, 128.63, 129.68, 131.65, 133.57, 134.08, 134.64, 140.00, 145.39, 159.46, 170.72.  $^{19}\text{F}$  NMR (acetone- $d_6$ )  $\delta$  -224.50 (m, 1F). MS for  $\text{C}_{22}\text{H}_{19}\text{FO}_5$ :  $m/z$  calcd 414.55; found 437.19 [ $\text{M} + \text{Na}$ ] $^+$ , 453.13 [ $\text{M} + \text{K}$ ] $^+$ . Anal. Calcd for  $\text{C}_{22}\text{H}_{19}\text{FO}_5$ : C, 63.76; H, 4.62. Found: C, 63.52; H, 4.44. HPLC: retention time 9.93 min, purity 98.02%.

**tert-Butyl 2-[2-(4'-Fluorobiphenyl-4-ylsulfonylethyl)phenyl]acetate (8).** The title compound was prepared starting from arylbromide 4 and 4-fluorophenylboronic acid following the same procedure used for compounds 5 and 6. The crude product was purified by flash



chromatography on silica gel (*n*-hexane/EtOAc 9:1) by use of an Isolute Si II cartridge (Biotage) to give a colorless oil (70% yield).

**tert-Butyl 2-[2-(4'-Aminobiphenyl-4-ylsulfonyl)phenyl]acetate (9).** The title compound was prepared starting from arylbromide **4** and 4-aminophenylboronic acid following the same procedure used for compounds **5** and **6**. The crude product was purified by flash chromatography on silica gel (*n*-hexane/EtOAc 4:1) by use of an Isolute Si II cartridge (Biotage) to give a foaming solid (75% yield).

**2-[2-(4'-Fluorobiphenyl-4-ylsulfonyl)phenyl]acetic acid (1b).** The title compound was prepared following the same procedure used for compound **1a**. The crude product was purified by trituration with Et<sub>2</sub>O and *n*-hexane to afford a white solid (63% yield). <sup>1</sup>H NMR, 500 MHz (acetone-*d*<sub>6</sub>) δ 4.11 (s, 2H); 7.29 (t, *J* = 8.31 Hz, 2H); 7.50–7.52 (m, 1H); 7.60–7.62 (m, 1H); 7.67–7.68 (m, 1H); 7.78 (dd, *J*<sub>1</sub> = 5.43 Hz, *J*<sub>2</sub> = 8.82 Hz, 2H); 7.87 (d, *J* = 8.32 Hz, 2H); 8.00 (d, *J* = 8.32 Hz, 2H); 8.21–8.23 (m, 1H). <sup>13</sup>C NMR, 500 MHz (acetone-*d*<sub>6</sub>) δ 37.57, 115.76, 115.93, 127.69, 127.96, 128.14, 129.35, 129.42, 129.66, 133.57, 134.00, 134.62, 135.38, 135.41, 136.76, 140.66, 162.20, 164.15, 170.69. <sup>19</sup>F NMR, 470 MHz (acetone-*d*<sub>6</sub>) δ –115.20 (m, 1F). MS for C<sub>20</sub>H<sub>15</sub>FO<sub>4</sub>S: *m/z* calcd 370.39; found 371.18 [M + H]<sup>+</sup>, 741.24 [2 M + H]<sup>+</sup>. Anal. Calcd for C<sub>20</sub>H<sub>15</sub>FO<sub>4</sub>S: C, 64.85; H, 4.08. Found: C, 63.73; H, 4.00. HPLC: retention time 10.1 min, purity 97.9%.

**tert-Butyl 2-[2-(4'-(2-Fluoroacetamido)biphenyl-4-ylsulfonyl)phenyl]acetate (10).** To a solution of compound **9** (134 mg, 0.32 mmol) in dry DMF (3.2 mL) was added *N,N*-diisopropylethylamine (71.6 μL, 0.95 mmol) and then fluoroacetyl chloride (0.95 mmol). The mixture was stirred at room temperature overnight, and then the reaction was taken up with water and the product was extracted with EtOAc. Organic layers were dried over Na<sub>2</sub>SO<sub>4</sub> and evaporated in vacuo. The crude product was purified by flash chromatography on silica gel (*n*-hexane/EtOAc 3:1) to afford a yellow oil (121 mg, 0.250 mmol, 78% yield).

**2-[2-(4'-(2-Fluoroacetamido)biphenyl-4-ylsulfonyl)phenyl]acetic Acid (1c).** The title compound was prepared following the same procedure used for compound **1a**. The crude product was purified by trituration with Et<sub>2</sub>O and *n*-hexane to afford a light brown solid (62% yield). <sup>1</sup>H NMR (DMSO-*d*<sub>6</sub>) δ 3.94 (s, 2H); 5.00 (d, <sup>3</sup>*J*<sub>H-F</sub> = 45.66 Hz, 2H); 7.43–7.45 (m, 1H); 7.57–7.59 (m, 1H); 7.65–7.68 (m, 1H); 7.72 (d, *J* = 8.75 Hz, 2H); 7.79 (d, *J* = 8.75 Hz, 2H); 7.88 (s, 4H); 7.95 (d, *J* = 8.05 Hz, 1H); 8.04 (br s, 1H) 8.09–8.11 (m, 1H); 10.24 (s, 1H). <sup>13</sup>C NMR (DMSO-*d*<sub>6</sub>) δ 38.41, 79.68, 81.10, 120.69, 127.74, 128.09, 128.30, 128.58, 128.97, 129.81, 130.57, 133.82, 134.22, 134.65, 134.89, 139.21, 139.38, 139.80, 144.94, 166.53, 166.68, 171.87. <sup>19</sup>F NMR (DMSO-*d*<sub>6</sub>) –225.14 (t, <sup>3</sup>*J*<sub>H-F</sub> = 45.66 Hz, 1F). MS for C<sub>22</sub>H<sub>18</sub>FNO<sub>5</sub>S: *m/z* calcd 427.45; found 450.20 [M + Na]<sup>+</sup>, 877.35 [2M + Na]<sup>+</sup>. Anal. Calcd for C<sub>22</sub>H<sub>18</sub>FNO<sub>5</sub>S: C, 61.82; H, 4.24; N, 3.28. Found: C, 61.60; H, 4.17; N, 3.33. HPLC: retention time 6.3 min, purity 97.8%.

**tert-Butyl 2-[2-(4'-(2-(Tosyloxy)ethoxy)biphenyl-4-ylsulfonyl)phenyl]acetate (11).** A suspension of phenol **6** (48 mg, 0.113 mmol), glycol-1,2-ditosylate (125.77, 0.339 mmol) and potassium carbonate (15.62 mg, 0.113 mmol) in CH<sub>3</sub>CN (3 mL) was refluxed under nitrogen atmosphere for 16 h. The mixture was then diluted with EtOAc and washed with water, and the combined organic phases were then dried over Na<sub>2</sub>SO<sub>4</sub> and evaporated in vacuo. The crude product was purified by flash chromatography on silica gel (*n*-hexane/EtOAc 4:1) by use of an Isolute Si II cartridge (Biotage) to yield a light brown solid (37.2 mg, 0.06 mmol, 53% yield). <sup>1</sup>H NMR (CDCl<sub>3</sub>) δ 1.36 (s, 9H); 2.42 (s, 3H); 3.93 (s, 9H); 4.18 (t, *J* = 5.13 Hz, 2H); 4.37 (t, *J* = 5.13 Hz, 2H); 6.86 (d, *J* = 8.79 Hz, 2H); 7.31–7.34 (m, 3H); 7.43–7.47 (m, 3H); 7.53–7.56 (m, 1H); 7.61 (d, *J* = 8.79 Hz, 2H); 7.80 (d, *J* = 8.06 Hz, 2H); 7.88 (d, *J* = 8.42 Hz, 2H). <sup>13</sup>C NMR (CDCl<sub>3</sub>) δ 21.73, 28.06, 29.77, 39.49, 65.66, 68.07, 81.34, 115.21, 127.31, 127.82, 128.09, 181.14, 128.56, 129.96, 133.44, 134.52, 139.42, 139.70, 145.09, 145.50, 158.65, 169.72. MS for C<sub>33</sub>H<sub>34</sub>O<sub>8</sub>S<sub>2</sub>: *m/z* calcd 622.75; found 645.30 [M + Na]<sup>+</sup>, 1267.42 [2M + Na]<sup>+</sup>. HPLC: retention time 20.28 min, purity 99.73%.

**tert-Butyl 2-[2-(4'-(2-Chloroacetamido)biphenyl-4-ylsulfonyl)phenyl]acetate (12).** The title compound was obtained starting from intermediate **9** and chloroacetyl chloride following the same

procedure used for compound **10**. The crude product was purified by flash chromatography on silica gel (*n*-hexane/EtOAc 3:1) to afford a yellow oil (70% yield). <sup>1</sup>H NMR (CDCl<sub>3</sub>) δ 1.36 (s, 9H); 3.93 (s, 2H); 4.20 (s, 2H); 7.31–7.33 (m, 1H); 7.44–7.48 (m, 1H); 7.55 (d, *J* = 8.79 Hz, 2H); 7.62–7.67 (m, 5H); 7.91 (d, *J* = 8.79 Hz, 2H); 8.15–8.17 (m, 1H); 8.31 (br s, 1H). <sup>13</sup>C NMR (CDCl<sub>3</sub>) δ 28.07, 39.50, 53.86, 81.40, 120.57, 127.58, 127.86, 128.12, 128.20, 129.97, 133.47, 133.60, 134.53, 135.95, 137.23, 139.30, 140.24, 145.17, 169.72. MS for C<sub>26</sub>H<sub>26</sub>ClNO<sub>3</sub>S: *m/z* calcd 500.01; found 522.16 [M + Na]<sup>+</sup>. HPLC: retention time 14.3 min, purity 98.2%.

**tert-Butyl 2-[2-(4'-(2-Bromoacetamido)biphenyl-4-ylsulfonyl)phenyl]acetate (13).** The title compound was obtained starting from intermediate **9** and bromoacetyl bromide following the same procedure used for compound **10**. The crude product was purified by flash chromatography on silica gel (*n*-hexane/EtOAc 5:1) by use of an Isolute Si II cartridge (Biotage) to afford a brown oil (57% yield).

**Radiosynthesis. Production of [<sup>18</sup>F]Fluoride Ions.** No-carrier-added (nca) [<sup>18</sup>F]fluoride was produced after irradiation of [<sup>18</sup>O]H<sub>2</sub>O by the <sup>18</sup>O(p, n)<sup>18</sup>F nuclear reaction in a 16.5 MeV cyclotron (PET Trace GE Medical System). The [<sup>18</sup>F]fluoride was delivered to the computer-controlled synthesizer Tracerlab FX<sub>FN</sub> (GE Medical System) and was passed through an anion-exchange resin (Sep-Pak Light Waters Accell Plus QMA cartridge). [<sup>18</sup>F]Fluoride ions were eluted from the resin in the reactor with a mixture of 22 mg of Kryptofix 2.2.2 (K 222) and 3 mg of K<sub>2</sub>CO<sub>3</sub> in 0.3 mL of ultrapure water and 0.3 mL of acetonitrile. Subsequently, the aqueous [<sup>18</sup>F]K(K 222)F solution was evaporated to dryness by azeotropic distillation at 90 °C in vacuo.

**tert-Butyl [<sup>18</sup>F]-2-[2-(4'-(2-Fluoroethoxy)biphenyl-4-ylsulfonyl)phenyl]acetate ([<sup>18</sup>F]-7).** Three milligrams of ethylene glycol ditosylate dissolved in 1 mL of acetonitrile and the dried [<sup>18</sup>F]K(K 222) residue were heated at 100 °C for 10 min in the reaction vessel of the synthesis module. Then the mixture was cooled, diluted with 4 mL of water for injection, and passed through a C18 Sep-Pak cartridge. The product was eluted with 2 mL of an acetonitrile/water mixture (3:2 v/v). After evaporation, a solution of 2 mg of **6** in 500 μL of DMSO/MeOH (4/1 v/v) and 0.28 mg of MeONa (10% excess) was added. The fluoroethylation was carried out at 120 °C for 12 min. The crude product was recovered without further purification, but the target compound accounted for only 10% of total radioactivity.

**[<sup>18</sup>F]-2-[2-(4'-(2-Fluoroethoxy)biphenyl-4-ylsulfonyl)phenyl]acetic Acid ([<sup>18</sup>F]-1a): One-Step Procedure.** Two milligrams of precursor **11** in 1 mL of acetonitrile was added to the dried [<sup>18</sup>F]K(K 222)F residue, and the mixture was heated at 105 °C for 10 min to allow the nucleophilic substitution. After cooling, the mixture was diluted with 10 mL of water and loaded on a C18 Sep-Pak cartridge for the intermediate purification step. The cartridge was washed with 2 mL of 10% EtOH and then eluted with 1.5 mL of 60% EtOH. After evaporation, a solution of 600 μL of TFA and 500 μL of acetonitrile was added and the deprotection was carried out at room temperature for 10 min. The mixture was diluted with 6 mL of water, loaded on a second C18 Sep-Pak cartridge, and washed with 2 mL of 10% EtOH. The cartridge was eluted with 1.5 mL of 60% EtOH. The following steps were performed manually. The final mixture was further purified by Oasis HLB plus cartridge: the cartridge was washed with 1 mL of 40% EtOH, and the product was finally eluted with 0.6 mL of 60% EtOH.

**[<sup>18</sup>F]-2-[2-(4'-(2-Fluoroacetamido)biphenyl-4-ylsulfonyl)phenyl]acetic Acid ([<sup>18</sup>F]-1c).** Three milligrams of precursor **12** in 1 mL of acetonitrile was added to the dried [<sup>18</sup>F]K(K 222)F residue. The mixture was heated at 130 °C for 12 min to allow the nucleophilic substitution. After cooling, the mixture was diluted with 6 mL of water and loaded on a C18 Sep-Pak cartridge for the intermediate purification step. The cartridge was washed with 2 mL of 10% EtOH and then eluted with 1.5 mL of EtOH. After solvent evaporation, a solution of 600 μL of TFA and 500 μL of acetonitrile was added and the deprotection was carried out at room temperature for 10 min. The solution was diluted with 6 mL of water, loaded on a second C18 Sep-Pak cartridge, and washed with 2 mL of 10% EtOH. The cartridge was finally eluted with 1.5 mL of EtOH. The final



ethanol solution was evaporated and the residue was diluted with phosphate buffer.

**MMP Inhibition Assay.** Recombinant human MMP-14 catalytic domain was a kind gift of Professor Gillian Murphy (Department of Oncology, University of Cambridge, U.K.). Pro-MMP-1, pro-MMP-2, pro-MMP-9, pro-MMP-3, and pro-MMP-13 were purchased from Calbiochem. Pro-MMP-12 was purchased from R&D Systems. Proenzymes were activated immediately prior to use with 2 mM *p*-aminophenylmercuric acetate (APMA): 2 mM for 1 h at 37 °C for MMP-2 and MMP-1, 1 mM for 1 h at 37 °C for MMP-9 and MMP-13. Pro-MMP-3 was activated with trypsin (5 µg/mL) for 30 min at 37 °C, followed by soybean trypsin inhibitor (SBTI) (62 µg/mL). Pro-MMP-12 was autoactivated by incubating in FAB buffer for 30 h at 37 °C. For assay measurements, the inhibitor stock solutions (DMSO, 10 mM) were further diluted, at seven different concentrations (0.01 nM–300 µM) for each MMP in the fluorometric assay buffer (FAB buffer: 50 mM Tris, pH = 7.5, 150 mM NaCl, 10 mM CaCl<sub>2</sub>, 0.05% Brij 35, and 1% DMSO). Activated enzyme (final concentration 0.5 nM for MMP-2, 1.3 nM for MMP-9, 0.3 nM for MMP-13, 5.0 nM for MMP-3, 1.0 nM for MMP-14, 2.0 nM for MMP-1, and 1.0 nM for MMP-12) and inhibitor solutions were incubated in the assay buffer for 4 h at 25 °C. After the addition of a 200 µM solution of the fluorogenic substrate Mca-Arg-Pro-Lys-Pro-Val-Glu-Nva-Trp-Arg-Lys-(Dnp)-NH<sub>2</sub> (Sigma) for MMP-3 and Mca-Lys-Pro-Leu-Gly-Leu-Dap(Dnp)-Ala-Arg-NH<sub>2</sub> (Bachem) for all other enzymes in DMSO (final concentration 2 µM), the hydrolysis was monitored every 15 s for 20 min, the increase in fluorescence ( $\lambda_{\text{ex}} = 325 \text{ nm}$ ,  $\lambda_{\text{em}} = 395 \text{ nm}$ ) was recorded on a Molecular Devices SpectraMax Gemini XS plate reader. The assays were performed in triplicate in a total volume of 200 µL/well in 96-well microtiter plates (Corning, black, NBS). Control wells lack inhibitor. The MMP inhibition activity was expressed in relative fluorescent units (RFU). Percent inhibition was calculated from control reactions without the inhibitor. IC<sub>50</sub> was determined from the formula  $v_i/v_0 = 1/(1 + [I]/\text{IC}_{50})$ , where  $v_i$  is the initial velocity of substrate cleavage in the presence of the inhibitor at concentration [I] and  $v_0$  is the initial velocity in the absence of inhibitor. Results were analyzed by use of SoftMax Pro 4.7.1 software (Molecular Devices) and GraFit 4 software (Erithecus Software).

**<sup>19</sup>F NMR Studies.** <sup>19</sup>F NMR spectra were acquired on a Bruker Avance III spectrometer operating at 11.7 T (corresponding to Larmor frequencies of 470 and 500 MHz for <sup>19</sup>F and <sup>1</sup>H, respectively), equipped with a double-resonance Z-gradient 5 mm BBFO probe, allowing for observation of the <sup>19</sup>F nucleus with decoupling of <sup>1</sup>H. Proton-decoupled <sup>19</sup>F NMR spectra were acquired with a 90° <sup>19</sup>F excitation pulse, spectral width of 220 ppm, 128K complex data points, and relaxation delay of 2.5 s. The number of scans was increased from 64 (free ligand) to 16 384 (protein:ligand 3:1) to get a suitable signal-to-noise ratio all over the titration. Sample temperature was kept at 310.0 K. Ligand (final concentration 1.0 mM) was dissolved in 50 µL of DMSO and brought to 1.0 mL with PBS (pH 7.4) containing 10% D<sub>2</sub>O for field/frequency lock. The solution also contained TFA as the <sup>19</sup>F NMR chemical shift internal standard ( $\delta = 0 \text{ ppm}$ ). Human serum albumin (fatty acid-free) was sequentially added to this solution, either in 10 µL aliquots (0.36 mM in PBS) or as the solid powder, up to protein:ligand ratio of 3:1.

**Cell Culture and Mouse U-87 MG Glioblastoma Tumor Model.** Human glioblastoma cells (U-87 MG) were supplied by ATCC (U-87 MG, ATCC HTB-14). ATCC has performed authentication and quality-control tests on the cell line according to Technical Bulletin 8. Cells were grown in Eagle's minimum essential medium (EMEM) supplemented with 10% fetal bovine serum, 2 mM glutamine, 100 IU/mL penicillin, and 100 µg/mL streptomycin. U-87 MG cells were collected and washed two times with PBS. Five million U-87 MG cells were resuspended in 0.1 mL of EMEM/Matrigel 1:1 and injected subcutaneously in the left flank of each 6-week-old female mouse. Tumor development was followed daily after inoculation by caliper measurement once the mass was established until the day of the PET experiment or sacrifice (typically within 10–15 days post-inoculation).

**Gelatin Zymography.** Tumors were removed from mice within 12 h from the PET scan and immediately frozen at –80 °C. Tumors were manually ground under dry ice and added to 50 µL of 1% Triton X-100 lysis buffer; the mixture was sonicated on ice, and the supernatant was collected by centrifugation (4 °C). An aliquot (20 µL) of the supernatant was mixed with sample buffer [250 mM Tris-HCl pH 6.8, 10% sodium dodecyl sulfate (SDS), 10% glycerol, and 0.4% bromophenol blue] and run on 10% SDS–polyacrylamide gel containing 0.1% gelatin at 150 V and room temperature for 85 min. The gel was washed twice (5 min) with distilled water, washed twice (30 min) with the renaturing buffer (50 mM Tris, 0.1 M NaCl, and 2.5% Triton X-100) to remove SDS, and rinsed twice (5 min) with deionized water. The gel was incubated for 24 h at 37 °C with the developing buffer consisting of 50 mM Tris-HCl, pH 7.4, 10 mM CaCl<sub>2</sub>, and 0.5 µM ZnCl<sub>2</sub>. After washings, gels were stained with 0.5% Coomassie blue. Gelatinolytic activity was identified as a white band on blue background. The 72 kDa band corresponds to MMP-2 and the 92 kDa band to MMP-9.

**In Situ DQ-Gelatin Zymography and Hematoxylin/Eosin Staining.** Six U-87 MG glioblastoma xenografts resected from mice that were not subjected to PET scans were frozen immediately after resection in isopentane/liquid nitrogen freezing bath and kept at –80 °C. Cryosections (10 µm thick) from vehicle- or ilomastat-treated tumors were serially cut for either in situ zymography or hematoxylin/eosin (HE) staining, transferred onto microscope slides, and air-dried for 30 min. DQ-gelatin (Enzcheck, Molecular Probes) was diluted in zymography buffer (50 mM Tris-HCl, 150 mM NaCl, and 0.2 mM sodium azide, pH 7.6) at a final concentration of 10 µg/mL, and sections were incubated at 37 °C for 30 min. As negative controls, DQ-gelatin was omitted or 10 mM 1,10-phenanthroline (Enzcheck, Molecular Probes) or 100 mM EDTA was added to the DQ-gelatin solution. After incubation, slides were fixed in 4% paraformaldehyde for 10 min, rinsed in PBS, and then mounted with Vectashield mounting medium (Vector Laboratories). Three fields per section were acquired by use of a confocal microscope (Leica SP5, Leica Microsystems), and the signal intensity was quantified with ImageJ software and normalized to the background.

For HE staining, 10-µm-thick cryosections were transferred onto microscope slides and air-dried for 30 min. After being rinsed in water, sections were stained with eosin for 30 s and hematoxylin for 1 min, dehydrated in increasing strengths of ethanol, and then cleared in xylene for 20 min. Slides were finally mounted with Eukitt mounting medium (Electron Microscopy Sciences), and images were acquired on a light microscope (Olympus BX51, Segrate, Italy).

**Western Blotting.** Six U-87 MG glioblastoma xenografts resected from mice that were not subjected to PET scans or treatment with MMP inhibitors were frozen immediately after resection in isopentane/liquid nitrogen freezing bath and kept at –80 °C. To extract proteins, each tumor was weighed, placed in a mortar, and finely powdered with a pestle in the presence of liquid nitrogen. The powder obtained was suspended in 0.5 mL of lysis buffer (50 mM Tris-HCl, pH 8, 150 mM NaCl, 1 mM EDTA, 100 mM KF, 10% glycerol, 1 mM MgCl<sub>2</sub>, 1% Triton X-100, and protease inhibitors), vortexed for 60 s, and then left on ice for 40 min. Afterward the solution was sonicated for few minutes and then centrifuged at 14000g at 4 °C for 10 min. The supernatant containing the soluble protein fraction was assayed for protein content by means of the BCA (bicinchoninic acid) method (Pierce, Thermo Fisher Scientific). Total extracts were diluted 1:1 in sample buffer (60 mM Tris-HCl, pH 6.8, 2% SDS, 10% glycerol, and bromophenol blue) and 20 µg/lane was loaded on a 10% polyacrylamide gel (Bio-Rad) to assay MMP-2; electrophoresis was performed under denaturing conditions with 2% β-mercaptoethanol. To obtain a standard calibration curve for the quantification, recombinant human MMP-2 (Calbiochem, Merck Millipore) was loaded in the same gel at concentrations of 10–20–40–60 ng. Proteins within the gel were transferred onto a nitrocellulose membrane (GE Healthcare) and the blotting was performed by incubation, after blocking for 1 h in 5% skim milk in Tris-buffered saline with Tween-20 (TBS-T: 10 mM Tris-HCl, pH 7.4, 0.1 M NaCl, and 0.1% Tween-20), with the antibodies of interest

(anti-MMP-2, Abcam) for 3 h at a concentration of 1  $\mu\text{g/mL}$  in 5% skim milk in TBS-T. The membrane was then rinsed in TBS-T for 1 h, incubated with the secondary antibody (peroxidase-conjugated goat anti-rabbit horseradish, Merck Millipore) at a concentration of 0.1  $\mu\text{g/mL}$  in 5% skim milk in TBS-T for 1 h, and rinsed again. Specific signal was visualized as a single or multiple band by the ECL detection method (enhanced chemiluminescence, GE Healthcare), based on the emission of light during the peroxidase-catalyzed oxidation of diacylhydrazide luminol. The emitted light is captured on a photographic film (Kodak, Sigma-Aldrich) for qualitative and semiquantitative analysis. Densitometric image analysis to evaluate the relative amount of protein staining was performed with Fiji-Win32 software.

**PET Images.** PET images were acquired on a YAP-(S)PET scanner (I.S.E. Ingegneria dei Sistemi Elettronici s.r.l., Pisa, Italy) designed for small animals.<sup>54</sup> Animals were anesthetized by inhalation of 0.5–2% isoflurane (100%  $\text{O}_2$ ), placed on the scanner bed in prone position, and injected in the tail vein (via catheter) with [ $^{18}\text{F}$ ]MMPi or [ $^{18}\text{F}$ ]fluoro-2-deoxyglucose ([ $^{18}\text{F}$ ]FDG) at a typical dose of 7.4 MBq (200  $\mu\text{Ci}$ , in 0.15–0.30 mL of PBS). The residual dose in the syringe was measured to verify the effective injected dose. For biodistribution studies, each tracer was tested on 2–3 healthy animals (nude mice 6–8 weeks old). Dynamic PET scans were performed from tracer injection up to 2.5 h to evaluate tracer distribution and to produce time–activity curves of liver, gut, kidneys, and gallbladder. Due to the detector's array dimension, only the part of the body within 4 cm and centered on the abdomen was imaged. At the end of the dynamic acquisition, a static acquisition (acquisition time 30 min) centered on the head of the animal was performed. PET images aimed at assessing tumor uptake of the [ $^{18}\text{F}$ ]labeled MMPi were performed when the tumor size reached a volume of 150–500  $\text{mm}^3$ . The PET scan was obtained by static acquisition (acquisition time 30 min) performed 100 min after the i.v. injection of [ $^{18}\text{F}$ ]MMPi (typically 7.4 MBq). At the end of [ $^{18}\text{F}$ ]MMPi static acquisition, the animal received 7.4 MBq of [ $^{18}\text{F}$ ]FDG via the catheter placed in the tail vein; care was taken not to move the animal. [ $^{18}\text{F}$ ]FDG PET scans (static mode, 30 min) were performed 45 min after tracer injection. For inhibition studies, ilomastat at a dose of 40–160 mg/kg was injected intraperitoneally 30 min before PET acquisition.

A 3D data acquisition mode and an expectation maximization (EM) algorithm with 30 iterations for image reconstruction were used; the resulting voxel size was  $0.5 \times 0.5 \times 2 \text{ mm}^3$ . No corrections were made for attenuation and scatter. The images were visualized with dedicated software (<http://www.pmod.com/>, last access 26/10/2011) in the three planes (transaxial, sagittal, and coronal). For semiquantitative evaluation, data from a 63 mL cylinder phantom-filled with [ $^{18}\text{F}$ ]fluoride (7.4 MBq) were acquired on the PET scanner and reconstructed with the same protocol used for the animal studies. From this scan, a system calibration factor was calculated by dividing the known activity concentration in the phantom by the measured mean counts per voxel in the reconstructed PET images. The calibration factor was used to convert the raw counts measured by the scanner into activity concentration. Region of interest (ROI) were manually drawn on the tumor/organ of interest in the transaxial images. [ $^{18}\text{F}$ ]Tracer uptake was corrected for decay and quantified by using the percentage injected dose per gram of tissue (% ID/g) calculated according to the expression

$$\% \text{ ID/g} = C_T \frac{V_T}{W_T} \frac{1}{D_{\text{inj}}} \times 100 \quad (1)$$

where  $C_T$  is the radioactivity in the ROI (in megabecquerels per milliliter of tissue),  $W_T$  (in grams) and  $V_T$  (in milliliters) are the mass and volume of the considered tissue (the  $V_T/W_T$  ratio has been assumed to be 1  $\text{mL/g}$ ; see ref 55), and  $D_{\text{inj}}$  is the injected dose of radiotracer (in megabecquerels).

## ■ ASSOCIATED CONTENT

### ■ Supporting Information

Two tables, listing inhibitor potency as  $K_i$  and % ID/g after tumor uptake of [ $^{18}\text{F}$ ]-1a and [ $^{18}\text{F}$ ]FDG; one figure with PET images showing passage of the tracers through the gallbladder; and additional text with analytical and spectroscopic data for compounds 2–10 and 13. This material is available free of charge via the Internet at <http://pubs.acs.org>.

## ■ AUTHOR INFORMATION

### Corresponding Author

\*(G.D.) Phone + 39 0131 360371, fax + 39 0131 360250, e-mail [giuseppe.digilio@mf.unipmn.it](mailto:giuseppe.digilio@mf.unipmn.it); (A.R.) phone + 39 050 2219562, fax + 39 050 2219605, e-mail [aros@farm.unipi.it](mailto:aros@farm.unipi.it).

### Author Contributions

▲F.C. and L.F. contributed equally to this work

### Notes

The authors declare no competing financial interest.

## ■ ACKNOWLEDGMENTS

We gratefully acknowledge Dr. Gabriele Dati (San Raffaele Scientific Institute, Milan), Dr. Juan Carlos Cutrin (Molecular Biotechnology Centre, Turin), and Dr. Claudio Cassino (DiSIT) for technical assistance and helpful discussion. Economic and scientific support from Regione Piemonte (Bando CIPE 2007 “Converging Technologies”) project “BIO\_THER: Modeling Oncogenic Pathways: from Bioinformatics to Diagnosis and Therapy”, from “Fondazione per le Biotecnologie” (FBT, Turin, Italy) and from Italian Ministry of University and Scientific Research (PRIN 2007, MIUR) is gratefully acknowledged.

## ■ ABBREVIATIONS USED

MMP, matrix metalloproteinases; ECM, extracellular matrix; TIMP, tissue inhibitor of metalloproteinase; MMPi, inhibitor of matrix metalloproteinase; ZBG, zinc binding group; HSA, human serum albumin; GIT, gastrointestinal tract; FDG, fluorodeoxyglucose; THF, tetrahydrofuran; DIPEA, *N,N*-diisopropylethylamine; TFA, trifluoroacetic acid; DMF, *N,N*-dimethylformamide; DMSO, dimethyl sulfoxide; DCM, dichloromethane; PEG, poly(ethylene glycol); EtOAc, ethyl acetate; RCY, radiochemical yield; RCP, radiochemical purity; EOS, end of synthesis; HE, hematoxylin and eosin; DQ, gelatin, dye-quenched gelatin; UR, uptake ratio; n.d.c., non decay corrected; EPR, Enhanced Permeability and Retention

## ■ REFERENCES

- (1) Massova, I.; Kotra, L. P.; Fridman, R.; Mobashery, S. Matrix metalloproteinases: structures, evolution, and diversification. *FASEB J.* **1998**, *12*, 1075–1095.
- (2) Nagase, H. H.; Woessner, J. F., Jr. Matrix metalloproteinases. *J. Biol. Chem.* **1999**, *274* (31), 21491–21494.
- (3) Hoekstra, R.; Eskens, F. A. L. M.; Verweij, J. Matrix metalloproteinase inhibitors: Current developments and future perspectives. *Oncologist* **2001**, *6*, 415–427.
- (4) Parks, W. C.; Wilson, C. L.; López-Boado, Y. S. Matrix metalloproteinases as modulators of inflammation and innate immunity. *Nat. Rev. Immunol.* **2004**, *4*, 617–229.
- (5) Egeblad, M.; Werb, Z. New functions for the matrix metalloproteinases in cancer progression. *Nat. Rev. Cancer* **2002**, *2*, 161–174.



- (6) Lampert, K.; Machein, U.; Machein, M. R.; Conca, W.; Peter, H. H.; Volk, B. Expression of matrix metalloproteinases and their tissue inhibitors in human brain tumors. *Am. J. Pathol.* **1998**, *153*, 429–437.
- (7) Sternlicht, M. D.; Bergers, G. Matrix metalloproteinases as emerging targets in anticancer therapy: status and prospects. *Emerging Ther. Targets* **2000**, *4*, 609–633.
- (8) Deryugina, E. I.; Quigley, J. P. Matrix metalloproteinases and tumor metastasis. *Cancer Metastasis Rev.* **2006**, *25*, 9–34.
- (9) López-Otín, C.; Palavalli, L. H.; Samuels, Y. Protective roles of matrix metalloproteinases: From mouse models to human cancer. *Cell Cycle* **2009**, *8* (22), 1–6.
- (10) Martin, M. D.; Matrisian, L. M. The other side of MMPs: Protective roles in tumor progression. *Cancer Metastasis Rev.* **2007**, *26*, 717–724.
- (11) Overall, C. M.; Kleinfeld, O. Tumor microenvironment e opinion: validating matrix metalloproteinases as drug targets and anti-targets for cancer therapy. *Nat. Rev. Cancer* **2006**, *6*, 227–239.
- (12) Whittaker, M.; Floyd, C. D.; Brown, P.; Gearing, A. J. H. Design and therapeutic application of matrix metalloproteinase inhibitors. *Chem. Rev.* **1999**, *99*, 2735–2776.
- (13) Hidalgo, M.; Eckhardt, S. G. Development of matrix metalloproteinase inhibitors in cancer therapy. *J. Natl. Cancer Inst.* **2001**, *93* (3), 178–193.
- (14) Scherer, R. L.; McIntyre, J. O.; Matrisian, L. M. Imaging matrix metalloproteinases in cancer. *Cancer Metastasis Rev.* **2008**, *27*, 679–690.
- (15) Yang, Y.; Hong, H.; Zhang, Y.; Cai, W. Molecular imaging of proteases in cancer. *Cancer Growth Metastasis* **2009**, *2*, 13–27.
- (16) Wagner, S.; Breyholz, H. J.; Faust, A.; Höltke, C.; Levkau, B.; Schober, O.; Schäfers, M.; Kopka, K. Molecular imaging of matrix metalloproteinases in vivo using small molecule inhibitors for SPECT and PET. *Curr. Med. Chem.* **2006**, *13*, 2819–2838.
- (17) Pimlott, S. L.; Sutherland, A. Molecular tracers for the PET and SPECT imaging of disease. *Chem. Soc. Rev.* **2011**, *40*, 149–162.
- (18) Cherry, S. R.; Sorenson, J. A.; Phelps, M. E. *Physics in Nuclear Medicine*, 3rd ed.; Saunders: Philadelphia, PA, 2003.
- (19) Kubota, K. From tumor biology to clinical PET: A review of positron emission tomography (PET) in oncology. *Ann. Nucl. Med.* **2001**, *6* (15), 471–486.
- (20) Cai, W.; Rao, J.; Gambhir, S. G.; Chen, X. How molecular imaging is speeding up antiangiogenic drug development. *Mol. Cancer Ther.* **2006**, *5* (11), 2624–2633.
- (21) Kopka, K.; Breyholz, H. J.; Wagner, S.; Law, M. P.; Riemann, B.; Schröer, S.; Trub, M.; Guilbert, B.; Levkau, B.; Schober, O.; Schäfers, M. Synthesis and preliminary biological evaluation of new radio-iodinated MMP inhibitors for imaging MMP activity in vivo. *Nucl. Med. Biol.* **2004**, *2* (31), 257–267.
- (22) Fei, X.; Zheng, Q.-H.; Liu, X.; Wang, J.-Q.; Stone, K. L.; Miller, K. D.; Sledge, G. W.; Hutchins, G. D. Synthesis of MMP inhibitor radiotracer [<sup>11</sup>C]CGS-25966, a new potential PET tumor imaging agent. *J. Label. Compd. Radiopharm.* **2003**, *46*, 343–351.
- (23) Wagner, S.; Breyholz, H.-J.; Law, M. P.; Faust, A.; Höltke, C.; Schröer, S.; Haufe, G.; Levkau, B.; Schober, O.; Schäfers, M.; Kopka, K. Novel fluorinated derivatives of the broad-spectrum MMP inhibitors *N*-hydroxy-2(R)-[[[(4-methoxyphenyl)sulfonyl](benzyl)- and (3-picolyl)-amino]-3-methyl-butanamide as potential tools for the molecular imaging of activated MMPs with PET. *J. Med. Chem.* **2007**, *50*, 5752–5764.
- (24) Wagner, S.; Breyholz, H.-J.; Höltke, C.; Faust, A.; Schober, O.; Schäfers, M.; Kopka, K. A new <sup>18</sup>F-labelled derivative of the MMP inhibitor CGS 27023A for PET: Radiosynthesis and initial small-animal PET studies. *Appl. Radiat. Isot.* **2009**, *67*, 606–610.
- (25) Van de Wiele, C.; Oltenfreiter, R. Imaging probes targeting matrix metalloproteinases. *Cancer Biother. Radiopharm.* **2006**, *21* (5), 409–417.
- (26) Furomoto, S.; Takashima, K.; Kubota, K.; Ido, T.; Iwata, R.; Fukuda, H. Tumor detection using <sup>18</sup>F-labeled matrix metalloproteinase-2 inhibitor. *Nucl. Med. Biol.* **2003**, *30*, 119–125.
- (27) auf dem Keller, U.; Bellac, C. L.; Li, Y.; Lou, Y.; Lange, P. F.; Ting, R.; Harwig, C.; Kappelhoff, R.; Dedhar, S.; Adam, M. J.; Ruth, T. J.; Bénard, F.; Perrin, D. M.; Overall, C. M. Novel matrix metalloproteinase inhibitor [<sup>18</sup>F]marimastat-aryltrifluoroborate as a probe for in vivo positron emission tomography imaging in cancer. *Cancer Res.* **2010**, *70*, 7562–7569.
- (28) Skiles, J. W.; Gonnella, N. C.; Jeng, A. Y. The design, structure and clinical update of small molecular weight metalloproteinase inhibitors. *Curr. Med. Chem.* **2004**, *11*, 2911–2977.
- (29) Breyholz, H.-J.; Wagner, S.; Faust, A.; Riemann, B.; Höltke, C.; Hermann, S.; Schober, O.; Schäfers, M.; Kopka, K. Radiofluorinated pyrimidine-2,4,6-triones as molecular probes for noninvasive MMP-targeted imaging. *ChemMedChem* **2010**, *5*, 777–789.
- (30) Nuti, E.; Panelli, L.; Casalini, F.; Avramova, S. I.; Orlandini, E.; Santamaria, S.; Nencetti, S.; Tuccinardi, T.; Martinelli, A.; Cercignani, G.; D'Amelio, N.; Maiocchi, A.; Uggeri, F.; Rossello, A. Design, synthesis, biological evaluation, and NMR studies of a new series of arylsulfones as selective and potent matrix metalloproteinase-12 inhibitors. *J. Med. Chem.* **2009**, *52*, 6347–6361.
- (31) Tuccinardi, T.; Martinelli, A.; Nuti, E.; Carelli, P.; Balzano, F.; Uccello-Barretta, G.; Murphy, G.; Rossello, A. Amber force field implementation, molecular modelling study, synthesis and MMP-1/MMP-2 inhibition profile of (R)- and (S)-*N*-hydroxy-2-(*N*-isopropoxybiphenyl-4-ylsulfonamido)-3-methylbutanamides. *Bioorg. Med. Chem.* **2006**, *14*, 4260–4276.
- (32) (a) Tamura, Y.; Watanabe, F.; Nakatani, T.; Yasui, K.; Fuji, M.; Komurasaki, T.; Tsuzuki, H.; Maekawa, R.; Yoshioka, T.; Kawada, K.; Sugita, K.; Ohtani, M. Highly selective and orally active inhibitors of type IV collagenase (MMP-9 and MMP-2): *N*-sulfonylamino acid derivatives. *J. Med. Chem.* **1998**, *41*, 640–649. (b) Kiyama, R.; Tamura, Y.; Watanabe, F.; Tsuzuki, H.; Ohtani, M.; Yodo, M. Homology modeling of gelatinase catalytic domains and docking simulations of novel sulfonamide inhibitors. *J. Med. Chem.* **1999**, *42*, 1723–1738.
- (33) Becker, D. P.; Barta, T. E.; Bedell, L. J.; Boehm, T. L.; Bond, B. R.; Carroll, J.; Carron, C. P.; DeCrescenzo, G. A.; Easton, A. M.; Freskos, J. N.; Funckes-Shippy, C. L.; Heron, M.; Hockerman, S.; Howard, C. P.; Kiefer, J. R.; Li, M. H.; Mathis, K. J.; McDonald, J. J.; Mehta, P. P.; Munie, G. E.; Sunyer, T.; Swearingen, C. A.; Villamil, C. I.; Welsch, D.; Williams, J. M.; Yu, Y.; Yao, J. Orally active MMP-1 sparing  $\alpha$ -tetrahydropyranyl and  $\alpha$ -piperidinyl sulfone matrix metalloproteinase (MMP) inhibitors with efficacy in cancer, arthritis, and cardiovascular disease. *J. Med. Chem.* **2010**, *53*, 6653–6680.
- (34) Whittaker, M.; Floyd, C. D.; Brown, P.; Gearing, A. J. Design and therapeutic application of matrix metalloproteinase inhibitors. *Chem. Rev.* **1999**, *99* (9), 2735–76.
- (35) Rao, J. S. Molecular mechanisms of glioma invasiveness: the role of proteases. *Nat. Rev. Cancer* **2003**, *3*, 489–501.
- (36) Kargiotis, O.; Chetty, C.; Gondi, C. S.; Tsung, A. J.; Dinh, D. H.; Gujrati, M.; Lakka, S. S.; Kyritsis, A. P.; Rao, J. S. Adenovirus-mediated transfer of siRNA against MMP-2 mRNA results in impaired invasion and tumor-induced angiogenesis, induces apoptosis in vitro and inhibits tumor growth in vivo in glioblastoma. *Oncogene* **2008**, *27*, 4830–4840.
- (37) Hagemann, C.; Anacker, J.; Haas, S.; Riesner, D.; Schömig, B.; Ernestus, R. I.; Vince, G. H. Comparative expression pattern of matrix-metalloproteinases in human glioblastoma cell-lines and primary cultures. *BMC Res. Notes* **2010**, *3*, 293–302.
- (38) Aime, S.; Digilio, G.; Bruno, E.; Mainero, V.; Baroni, S.; Fasano, M. Modulation of the antioxidant activity of HO<sup>•</sup> scavengers by albumin binding: a <sup>19</sup>F NMR study. *Biochim. Biophys. Res. Commun.* **2003**, *307*, 962–966.
- (39) Mao, H.; Hajduk, P. J.; Craig, R.; Bell, R.; Borre, T.; Fesik, S. W. Rational design of diflunilal analogues with reduced affinity for human serum albumin. *J. Am. Chem. Soc.* **2001**, *123* (43), 10429–10435.
- (40) Ghuman, J.; Zunsain, P. A.; Petitpas, I.; Bhattacharya, A. A.; Ottagiri, M.; Curry, S. Structural basis of the drug-binding specificity of human serum albumin. *J. Mol. Biol.* **2005**, *353*, 38–52.
- (41) Prante, O.; Tietze, R.; Hocke, C.; Löber, S.; Harald, H.; Kuwert, T.; Gmeiner, P. Synthesis, radiofluorination, and in vitro evaluation of



pyrazolo[1,5-*a*]pyridine-based dopamine D4 receptor ligands: discovery of an inverse agonist radioligand for PET. *J. Med. Chem.* **2008**, *51*, 1800–1810.

(42) Snoek-van Beurden, P. A. M.; Von den Hoff, J. W. Zymographic techniques for the analysis of matrix metalloproteinases and their inhibitors. *BioTechniques* **2005**, *38*, 73–83.

(43) Sprague, J. E.; Li, W. P.; Liang, K.; Achilefu, S.; Anderson, C. J. In vitro and in vivo investigation of matrix metalloproteinase expression in metastatic tumor models. *Nucl. Med. Biol.* **2006**, *33*, 227–237.

(44) Nakada, M.; Nakamura, H.; Ikeda, E.; Fujimoto, N.; Yamashita, J.; Sato, H.; Seiki, M.; Okada, Y. Expression and tissue localization of membrane-type 1, 2, and 3 matrix metalloproteinases in human astrocytic tumors. *Am. J. Pathol.* **1999**, *154*, 417–428.

(45) Somiari, S. B.; Somiari, R. I.; Heckman, C. M.; Olsen, C. H.; Jordan, R. M.; Russell, S. J.; Shriver, C. D. Circulating MMP2 and MMP9 in breast cancer—Potential role in classification of patients into low risk, high risk, benign disease and breast cancer categories. *Int. J. Cancer* **2006**, *119*, 1403–1411.

(46) Eckelman, W. The application of receptor theory to receptor-binding and enzyme-binding oncologic radiopharmaceuticals. *Nucl. Med. Biol.* **1994**, *21*, 759–769.

(47) Woessner, J. F., Jr. Quantification of matrix metalloproteinases in tissue samples. *Methods Enzymol.* **1995**, *248*, 510–528.

(48) Fukuda, H.; Furumoto, S.; Iwata, R.; Kubota, K. New radiopharmaceuticals for cancer imaging and biological characterization using PET. *Int. Congr. Ser.* **2004**, *1264*, 158–165.

(49) Galaray, R. E.; Cassabonne, M. E.; Giese, C.; Gilbert, J. H.; Lapierre, F.; Lopez, Schaeffer, M. E.; Stack, R.; Sullivan, M.; Summers, B.; Tressler, R.; Tyrrell, D.; Wee, J.; Allen, S. D.; Castellet, J. J.; Barletta, J. P.; Schultz, G. S.; Fernandez, L. A.; Fisher, S.; Cui, T.-Y.; Foellmer, H. G.; Grobelny, D.; Holleran, W. M. Low molecular weight inhibitors in corneal ulceration. *Ann. N.Y. Acad. Sci.* **1994**, *732*, 315–323.

(50) Gringeri, C. V.; Menchise, V.; Rizzitelli, S.; Cittadino, E.; Catanzaro, V.; Dati, G.; Chaabane, L.; Digilio, G.; Aime, S. Novel Gd(III)-based probes for MR molecular imaging of matrix metalloproteinases. *Contrast Media Mol. Imaging* **2012**, *7* (2), 175–184.

(51) Hugenberg, V.; Breyholz, H.-J.; Riemann, B.; Hermann, S.; Schober, O.; Schäfers, M.; Gangadharmath, U.; Mocharla, V.; Kolb, H.; Walsh, J.; Zhang, W.; Kopka, K.; Wagner, S. *J. Med. Chem.* **2012**, *55*, 4714–4727.

(52) Zheng, Q.-H.; Fei, X.; DeGrado, T. R.; Wang, J.-Q.; Stone, K. L.; Martinez, T. D.; Gay, D. J.; Baity, W. L.; Mock, B. H.; Glick-Wilson, B. E.; Sullivan, M. L.; Miller, K. D.; Sledge, G. W.; Hutchins, G. D. Synthesis, biodistribution and micro-PET imaging of a potential cancer biomarker carbon-11 labeled MMP inhibitor (2*R*)-2-[[4-(6-fluorohex-1-ynyl)phenyl]sulfonylamino]-3-methylbutyric acid [<sup>11</sup>C]-methyl ester. *Nucl. Med. Biol.* **2003**, *30*, 753–760.

(53) Waschku, B.; Faust, A.; Schäfers, M.; Bremer, C. Performance of a new fluorescence-labeled MMP inhibitor to image tumor MMP activity in vivo in comparison to an MMP-activatable probe. *Contrast Media Mol. Imaging* **2013**, *8*, 1–11.

(54) Del Guerra, A.; Bartoli, A.; Belcari, N.; Herbert, D. J.; Motta, A.; Vaiano, A.; Di Domenico, G.; Sabba, N.; Moretti, E.; Zavattini, G.; Lazzarotti, M.; Sensi, L.; Larobina, M. Performance evaluation of the fully engineered YAP-(S)PET scanner for small animal imaging. *IEEE Trans. Nucl. Sci.* **2006**, *53* (3), 1078–1083.

(55) Phelps, M. E. *PET: Molecular Imaging and Its Biological Applications*; Springer-Verlag: New York, 2004.